Transactions in Theoretical and Mathematical Physics

Publisher: Qom University of Technology

ISSN: 3041-8984

Volume**:** 1, Issue 3, 2024

Available online: https://ttmp.qut.ac.ir

Table of Contents

TTMP vol 1(3), 2024
doi: 10.30511/TTMP.2024.202 590.1024

Transactions in Theoretical and Mathematical Physics

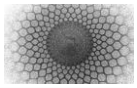

Concept of weak derivative by resorting to physical examples

Mehdi Jafari Matehkolaee[a,1], Alireza Hoseinian Abarghoei[2]

[1] Department of Physics and Energy Engineering, Amirkabir University of Technology (Tehran Polytechnic), Hafez Avenue, Tehran, Iran
[2] Department of Mechanical Engineering, Amirkabir University of Technology (Tehran Polytechnic), Iran

Received: 15 April 2024 / Accepted: 01 May 2024 / Published: August 2024

Abstract In this article, we present the concept of weak derivatives with respect to the potential of a charge distribution. Furthermore, weak derivatives can define the correct self-adjoint momentum operators in quantum mechanics.

1 Introduction

The concept of weak derivative can be considered a generalization of the classical derivative. In other words, functions that are not differentiable but are capable of integration can have weak derivatives [1].

Most studies on weak derivatives are associated with a subspace of Hilbert space, such as Sobolev space [1-5]. This coincidence could be more pleasant for popular physicists unfamiliar with functional analysis, so we try to address this topic with a newer and more impressive approach.

In ref. [4], it has been discussed how to define weak and strong derivatives in Orlicz space (Orlicz space is a special subspace of Banach space; if we define Banach space by L^p, the Orlicz space is determined by $p = 1$). The relationship between perturbation analysis and weak derivative is analyzed in ref [5].

We didn't find any paper that directly indicates the exact application of the weak derivative in physics. However, paper [6] endeavours to indicate its contribution to understanding mathematical models. The weak derivative also motivates another quite popular concept of solutions, the so-called weak solutions [6, 7].

The definition of the weak derivative can be stated as follows: Let f be a function in the measurable space (A real or complex-valued measurable function on the real line with respect to Lebesgue measure is an element of L^1 if: $\int_{-\infty}^{\infty}|f(x)|\,dx < \infty$), we call the function f in $L'([a,b])$ the weak derivative of f if

$$\int f(x)g(x)dx = \int f'(x)g(x)dx, \qquad (1)$$

In equation (1), $f'(x)$ is the weak derivative of $f(x)$ and the function $g(x)$ is called test function. These test functions are smooth and have bounded support. Note that, the test function is infinitely differentiable and $g \in C_c^{\infty}$.

The most common examples of functions with a weak derivative are the absolute value function $f(x) = |x|$, whose weak derivative is the sign function, and the Heaviside step function, whose derivative is the delta function.

2 Concept of weak derivative

Unlike the classical concept of derivative, which has a geometric concept, the weak derivative has no geometric concept. However, this can be described in relation to the concept of distribution.

First, note that one way to identify the function f with a given domain is to know the value of $f(x)$ for each x in the domain of the function f. But there is another way. Knowledge of the effect of function f on test functions. For example, in

$$(f,g) = \int f(x)g(x)dx. \qquad (2)$$

It is possible to find the effect of f' in the situation where f' exists or does not exist in the usual way, in other words $(f',g) = -(f,g')$. Now, for a physical understanding, let's assume that $f(x)$ is the potential of a point charge which we know is inversely proportional to the distance

[a] m.matehkolaee@aut.ac.ir

$$\int V(x)g(x)dx = \int \frac{1}{x} g(x)dx. \quad (3)$$

The potential function has no weak derivative, but if we consider the potential function of the linear charge distribution to be like an infinite bar, that is

$$\int V(x)g(x)dx = \int ln(x)\, g(x)dx. \quad (4)$$

In this case, we will see a weak derivative and the electric field can be investigated. First, consider the following example.

Example 1

Suppose the function $f(x)$ is defined by

$$f(x) = \begin{cases} \frac{1}{x} & x > 0 \\ 0 & x < 0 \end{cases}, \quad (5)$$

Let's now look at the following test function, which is smooth and has bounded support.

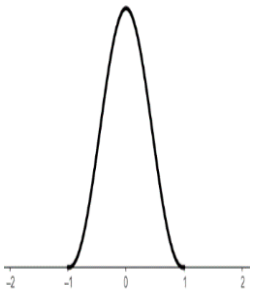

Figure 1. The desired test function is a smooth function that is differentiable, usually several times.

Then, with respect to the definition (1), we can write

$$\int_0^\infty \left(\frac{1}{x}\right) g(x)dx = \frac{g(\infty)}{\infty} - \frac{g(0)}{0} + \int_0^\infty \left(\frac{1}{x^2}\right) g(x)dx. \quad (6)$$

In equation (6), if the value of $g(0)$ is equal to zero, then there exists a weak derivative of the function (5), but otherwise it is not equal to zero, there will be no weak derivative. According to the definition and representation of the mentioned test function, the value of $g(0)$ can not be zero, so the weak derivative of the function $f(x)$ does not exist.

Example 2

Consider the function $h(x)$ with the following definition

$$f(x) = \begin{cases} \ln(x) & x > 0 \\ 0 & x < 0 \end{cases}. \quad (7)$$

We consider the test function again, as in the previous example. Here we will see that there is $\int h(x)g(x)dx$ for any test function g.

To evaluate the integral, we can write

$$\int h(x)g'(x)\, d\, x = \int_0^\infty (ln(x))\, g'(x)\, d\, x$$

$$= \lim_{s\to 0^+} ln(s)g(s) + \int_s^\infty \left(\frac{1}{x}\right) g(x)\, d\, x. \quad (8)$$

Although each of the above expressions tends to infinity independently in the limit $s \to \infty$, but their sum tends to a certain value (if $g(0) \neq 0$). Therefore, there exists a weak derivative of $h(x)$.

3 The electrical potential of an infinite line of charge

In this section, we obtain the electric field due to the weak derivative of an infinite uniform charge line. Before that, we will discuss an important property of the delta function.

From mathematical physics textbooks, the delta function has many properties. However, one advanced but notable characteristic associated with this function is related to the equation, which states that it $x\delta(x)$ is identically zero. As a result, we may add any finite multiple of this zero to one side of the equation.

$$A(x) = B(x) = B(x) + c\, x\, \delta(x), \quad (9)$$

where c is an arbitrary finite constant. However, if we divide both sides by x, the addition $c\, \delta\, (x)$ is no longer to zero at $x = 0$. Then

$$\frac{A(x)}{x} = \frac{B(x)}{x} + c\, \delta\, (x), \quad (10)$$

is not necessarily true for arbitrary values of c.
For example, consider

$$x\frac{d\, ln(x)}{dx} = 1 = 1 + c\, x\, \delta(x), \quad (11)$$

is valid for any constant c. However,

$$\frac{d\,ln(x)}{dx} = \frac{1}{x} + c\,\delta(x). \tag{12}$$

This is true for any special values of c.To determine these values, we need to examine the behavior of these functions in the neighborhood of $x = 0$ by integrating both sides of the expression (12) from $-\varepsilon$ to ε. Thus $c = i(2n+1)\pi$, where n is any integer.
An equation similar to Eq. (12) can be seen in [8]. As this reference shows, this equation is not just a mathematical curiosity. It plays an important role in quantum mechanics.
Let us now return to the potential of an infinite line of charge. We know that the potential of an infinite bar with charge density λ at vertical distance y is equal to

$$V = \frac{\lambda}{2\pi\varepsilon_0} ln(y) = \begin{cases} \frac{\lambda}{2\pi\varepsilon_0} ln(y) & y > 0 \\ 0 & y < 0 \end{cases}. \tag{13}$$

Thus, with respect to the Eq. (12), the electric field can be written

$$E = \frac{-\lambda}{2\pi\varepsilon_0}\left(\frac{1}{y} + i(2n+1)\pi\delta(y)\right). \tag{14}$$

Eq. (14) shows that despite the singularity, we can obtain an identified electric field at the location of the electric charge.

Note that although the weak derivative of Eq. (13) does exist, the electric field of (14) is not exactly its weak derivative.

4 The Weak derivative in quantum mechanics

The momentum operator in quantum mechanics is an unbounded operator, and its domain in $L^2(\mathbb{R}, dx)$ is equal to

$$D(P) = \{\varphi(x) \in L^2(\mathbb{R}, dx) | \varphi'(x) \in L^2(\mathbb{R}, dx)\}. \tag{15}$$

Eq. (15) states that the domain of momentum operators consisting of square-integrable functions must be differentiable, and their derivatives must lie in Hilbert space. However, there are some examples, such as

$$f(x) = \frac{x^{\frac{1}{3}}}{1+x^2}, \tag{16}$$

which despite being square-integrable but its derivative is not in $L^2(\mathbb{R}, dx)$. Also, there is another problem.

For functions such as $f(x)$ and $g(x)$ belonging to the domain of the momentum operator, we can write:

$$(g, Pf) - (Pg, f) = [-ig^* f]_{-\infty}^{+\infty}. \tag{17}$$

Normally the functions f and g are considered to be zero in the $lim\, x \to \pm\infty$, but the reality is that not all square-integrable functions vanish or even tend to reach a finite value at infinity. We can see plenty of examples in [9, 10] to confirm this point.

Thus, in general, the momentum operator is not self-adjoint with its common definition based on the concept of classical derivative [10]. For this reason, this operator is defined based on the weak derivative [11]. In this case, the domain of the momentum operator coincides with the Sobolev space $H^1(\mathbb{R})$ [11]. This is very impressive, every function in Sobolev space tends to zero at infinity [12]. Therefore, the correct domain of the momentum operators in quantum mechanics can be as follows

$$D(P) = \{\varphi(x) \in L^2(\mathbb{R}, dx) | \varphi'(x) \in L^2(\mathbb{R}, dx)\}, \tag{18}$$

where $\varphi'(x)$ is the weak derivative of the function $\varphi(x)$.

All of the mentioned discussions in this section have been examined for the generalized momentum operators in ref. [13].

5 Conclusion

Although the weak derivative has no geometric description, as we have seen, it is possible to express concepts related to distribution functions. We have chosen two examples related to the potential of the charge point and the linear distribution of charge. The weak derivative of the first example does not exist in the singularity but in the second example.

In standard quantum mechanics, momentum operators are generally not self-adjoint. This subject led mathematical physicists to propose subspaces such as Sobolev space. In this space, the weak derivative determines the momentum operators with a new domain. As discussed in the last section, the discussion about the self-adjointness of momentum operators moved on to the generalized momentum operators. For these operators, see the ref. [14] and the references therein.

References

1. J. Jost, *Postmodern Analysis* (Springer, Berlin, Heidelberg, 1998)
2. W. P. Ziemer, *Weakly Differentiable Functions* (Springer, 1989)
3. A. K. Nandakumaran, P. S. Datti, *Partial Differential Equations, Classical Theory with a Modern touch* (Cambridge University Press, 2020)
4. J. P. Gossez, Bull. de la Classe des sc. **67** (1981)
5. B. Heidergott and X. R. Cao, IEEE Trans. Automat. Contr. **47**, 7 (2002)
6. A. Eikmier, E. Emmerich, E. Schöll, Int. J. Dynam. Control, **6** (2018)
7. G. B. Lieberman, *Oblique Derivative Problems for Elliptic Equations* (World Scientific, 2013)
8. P. A. M. Dirac, *The Principle of quantum mechanics, Fourth Edition* (Oxford university press, 1957)
9. Q. Teschi, *Mathematical methods in Quantum mechanics, with applications to Schrödinger operators* (American Mathematical Society, 2014)
10. F. Gieres, Rep. . Prog. in Phy. **63**, 12 (2001).
11. M. Valter, Int. J. Geom. Meth. Mod. Phys. **13** (2016)
12. H Brezis, *Functional analysis, Sobolev spaces and partial differential equations* (Springer, 2011).
13. M. Jafari Matehkolaee, Pramana J. Phys. **95** (2021).
14. M. Jafari Matehkolaee, Z. Norouzbeh, Trans. Th. Math. Phy. **1**, (2) 2024

TTMP vol 1(3), 2024
doi: 10.30511/TTMP.2024.2035804.1029

Transactions in Theoretical and Mathematical Physics

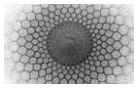

Determination of infinitesimal generators on de Sitter space-time

Ardeshir Rabeie[a]

Department of Physics, Razi University, Kermanshah

Received: 15 April 2024 / Accepted: 01 May 2024 / Published: 14 August 2024

Abstract In this work, we study the motion of a free particle in 1+3-de Sitter spacetime and introduce the associated symmetric group. We also present ten one-parameter subgroups of this group and derive the corresponding algebraic bases (or the Lie algebra of the de Sitter group). Finally, these subgroups introduce ten associated infinitesimal generators in 1+3-de Sitter spacetime.

1 Introduction

In general relativity, gravity is considered as the curvature of space-time, and the motion of a particle in this space is expressed by Einstein's equation [1]:

$$G_{\mu\nu} + \lambda g_{\mu\nu} = -T_{\mu\nu}\,, \tag{1}$$

where $T_{\mu\nu}$ and λ are the energy-momentum tensor and cosmological constant, respectively. From this equation, we can derive one of the Friedmann-Lemaitre-Robertson-Walker solutions for a homogeneous and isotropic universe [2]:

$$H_\circ{}^2 = \frac{\lambda}{3} + \frac{8\pi G}{3}\rho - \frac{K}{a^2}, \qquad H_\circ = \frac{\dot{a}}{a}, \tag{2}$$

where $H_\circ, G, a$ and K are respectively the Hubble parameter, Gravitational constant, scale factor and curvature of the universe. This equation can be rewritten by density parameters as:

$$\Omega_\lambda + \Omega_{other} = 1, \tag{3}$$

where Ω_λ is the density of Gravitational constant or density of dark energy[1] and Ω_{other} includes the densities of radiation (Ω_r), (cold) dark matter (Ω_c), baryonic matter (Ω_b) and curvature of space (Ω_K) [2]. Eq. (3) can be used for different epochs of cosmology [2,3]. For the current epoch, the experimental data show that approximately 69% of the universe is made up of dark energy, and the contribution of other factors[2] is 31% [4]. This means that for an approximate solution to Einstein's equation, we can consider only the cosmological constant and ignore the energy-momentum tensor on the right-hand side of Eq. (1). In other words, in the first approximation, the universe can be considered as a 1+3-de-Sitter space (i.e., the case $\lambda > 0$ and $T_{\mu\nu} = 0$ in Eq. (1)).

The 1+3-de Sitter metric is visualised as a hyperboloid embedded in five-dimensional Minkowski space. It is very important to study the symmetrical group associated with the motion of a free particle on this hyperboloid and its Lie algebra, which we discuss in this work. We also introduce all infinitesimal generators on this manifold.

2 1+3-de Sitter space-time

The de Sitter metric $g_{\mu\nu}$ is the solution of Einstein's equation for $\lambda > 0$ and $T_{\mu\nu} = 0$, i.e.

$$G_{\mu\nu} + \lambda g_{\mu\nu} = 0. \tag{4}$$

[a] e-mail: rabeie@razi.ac.ir

[1] The cosmological constant can be considered as the dark energy (see chapter 6 of [2]).

[2] The Ω_{other} is given by:
$\Omega_{other} = \Omega_r + \Omega_c + \Omega_b + \Omega_K$,
where constitutes 31% of the universe (for thecurrent epoch).
The contribution of each factor is as follows [2]:
$\Omega_r \to 0.008\% \Omega_c \to 26.07\%$
$\Omega_b \to 04.90\% \Omega_K \to 0.07\%$

The 1+3-de Sitter space-time as a hyperboloid embedded in five-dimensional Minkowski space (ambient space) is defined by:

$$X \equiv \{x \in \mathbb{R}^5 | x^2 = \eta_{\gamma\beta} x^\gamma x^\beta = -H_\circ^{-2}\}, \quad (5)$$

where $\eta_{\gamma\beta} = diag(1,-1,-1,-1,-1)$ is Minkowski metric of five-dimensional space and $\gamma, \beta = 0,1,2,3,4$. The associated isometry group is group $SO_0(1,4)$, or equivalently its universal covering, i.e. the symplectic group $Sp(2, 2)$. The group $SO_0(1,4)$ is defined as:

$$SO_0(1,4) = \{\Lambda \in M_5(R) | \Lambda^{00} \geq 1, \Lambda^t \eta \Lambda = \eta\}. \quad (6)$$

This group acts on the vector x in ambient space as follows:

$$x' = \Lambda x, \quad (7)$$

where $x = \begin{pmatrix} x^0 \\ x^1 \\ x^2 \\ x^3 \\ x^4 \end{pmatrix}$.

But the $Sp(2,2)$ group is described by 2×2 matrices with quaternionic[3] coefficients as [5]:

$$Sp(2,2) = \left\{ g = \begin{pmatrix} a & b \\ c & d \end{pmatrix} | det\ g = 1, g^\dagger \gamma^0 g = \gamma^0 \right\}, \quad (8)$$

where a, b, c, d belong to quaternion field $Q \simeq \mathbb{R}_+ \times SU(2)$ and $\gamma^0 = \begin{pmatrix} I & 0 \\ 0 & -I \end{pmatrix}$ that I and 0 are respectively 2×2 unit and zero matrices. This group acts on matrix h as:

$$h' = ghg^{-1}, \quad (9)$$

where

$$h = \begin{pmatrix} x^0 I - P \\ \overline{P} - x^0 I \end{pmatrix}, g^{-1} = \begin{pmatrix} \overline{a} & -\overline{c} \\ -\overline{bd} \end{pmatrix}, P = \begin{pmatrix} x^4 + ix^3 & ix^1 - x^2 \\ ix^1 + x^2 & x^4 - ix^3 \end{pmatrix},$$

and the bar sign means conjugate. Between two mentioned groups, there is a homomorphism as follows:

$$\Lambda_\beta^\alpha = \frac{1}{4} tr(\gamma^\alpha g \gamma_\beta g^{-1}), \quad (10)$$

Where $\gamma^4 = \begin{pmatrix} 0 & I \\ -I & 0 \end{pmatrix}, \gamma^k = \begin{pmatrix} 0 & e_k \\ e_k & 0 \end{pmatrix}, k = 1,2,3,$
and $e_k = (-1)^{k+1} i\sigma_k$. The σ_k is one of the three Pauli matrices. In the following, we only use the group $Sp(2,2)$.

3 Lie algebra of de Sitter group

The study of Lie algebra and, consequently, the infinitesimal generators of a group is done by decomposing every element of that group. There are three decompositions for presentation of $Sp(2,2)$ group. The Lorentz space-time, Kartan and Ivasava decompositions [6]. Here, we use the first decomposition. Based on the Lorentz space-time decomposition, each element of $Sp(2,2)$ group is given as [5]:

$$g = jl \in Sp(2,2), \quad (11)$$

$$j = \begin{pmatrix} \eta & 0 \\ 0 & \bar{\eta} \end{pmatrix} \begin{pmatrix} cosh(\frac{\psi}{2}) & sinh(\frac{\psi}{2}) \\ sinh(\frac{\psi}{2}) & cosh(\frac{\psi}{2}) \end{pmatrix}, \quad (12)$$

$$l = \begin{pmatrix} \xi & 0 \\ 0 & \xi \end{pmatrix} \begin{pmatrix} cosh(\frac{\varphi}{2}) & \hat{u}\, sinh(\frac{\varphi}{2}) \\ -\hat{u}\, sinh(\frac{\varphi}{2}) & cosh(\frac{\varphi}{2}) \end{pmatrix}, \quad (13)$$

where $\varphi, \psi \in \mathbb{R}$, $\eta, \xi \in SU(2)$ and $\hat{u}$ is a pure quaternion i.e., $\bar{\hat{u}} = -\hat{u} \in SU(2)$. The factors j and l belong to the set of space-time translation and the homogeneous Lorentz subgroup (including the Lorentz boost and spatial rotation), respectively. This shows that the group $Sp(2,2)$ has ten parameters (three for space translation, one for time translation, three for spatial rotation and three for Lorentz boost). Therefore, we have ten one-parameter subgroup as:

$$S_i = \begin{pmatrix} e^{e_i t} & 0 \\ 0 & e^{-e_i t} \end{pmatrix}, \quad (14)$$

$$\Theta = \begin{pmatrix} cosh(\frac{t}{2}) & sinh(\frac{t}{2}) \\ sinh(\frac{t}{2}) & cosh(\frac{t}{2}) \end{pmatrix}, \quad (15)$$

$$R_i = \begin{pmatrix} e^{e_i t} & 0 \\ 0 & e^{e_i t} \end{pmatrix}, \quad (16)$$

[3] Every quaternion is given by:
$\zeta = (\zeta_0, \vec{\zeta}) = \zeta_0 + \zeta_1 e_1 + \zeta_2 e_2 + \zeta_3 e_3$,
where
$e_i e_j = \varepsilon_{ijk} e_k i, j, k = 1,2,3$,
$e_j e_j = -1$.

$$B_i = \begin{pmatrix} cosh(\frac{t}{2}) & e_i\, sinh(\frac{t}{2}) \\ -e_i\, sinh(\frac{t}{2}) & cosh(\frac{t}{2}) \end{pmatrix}, \quad (17)$$

and ten corresponding algebraic bases:

$$X_{i4} = \frac{1}{2}\begin{pmatrix} e_i & 0 \\ 0 & -e_i \end{pmatrix}, \quad (18)$$

$$X_{04} = \frac{1}{2}\begin{pmatrix} 0 & I \\ I & 0 \end{pmatrix}, \quad (19)$$

$$X_{ij} = \frac{1}{2}\varepsilon_{ijk}\begin{pmatrix} e_k & 0 \\ 0 & e_k \end{pmatrix}, \quad (20)$$

$$X_{0i} = \frac{1}{2}\begin{pmatrix} 0 & e_i \\ -e_i & 0 \end{pmatrix}, \quad (21)$$

Where t is a parameter, and $i, j, k = 1,2,3$.

4 Infinitesimal generators of de Sitter group

For determination of the infinitesimal generators of de Sitter group (or equivalently on hyperboloid manifold), we have to first introduce the generator (operator) $\ell^{\tau}(g)$. This operator acts on complex function $F(\zeta) \in \mathbb{C}$ on Hilbert subspace $H = L_c^2(SU(2))$ as [7]:

$$\begin{aligned} \ell^{\tau}(g)F(\zeta) &= (\chi(\zeta, g))^{-2\tau}F(g^{-1}.\zeta) \\ &= (\chi(\zeta, g))^{-2\tau}F((a'\zeta + b')(c'\zeta + d')^{-1}), \end{aligned} \quad (22)$$

where $\chi(\zeta, g) = det(\, c'\zeta + d')$, $\zeta \in SU(2)$, and

$$g^{-1} = \begin{pmatrix} a' & b' \\ c' & d' \end{pmatrix}.$$

Indeed, the mapping $\zeta \to g^{-1}.\zeta = (a'\zeta + b')(c'\zeta + d')^{-1}$ is a homomorphism mapping from $SU(2)$ group to itself. The representation of (22) is a linear representation. This representation is the unitary representation of the principal series if and only if

$$\tau = \frac{3}{2} + i\nu, \quad \nu \in \mathbb{R}. \quad (23)$$

Now we construct the representation of each one parameter subgroup of $Sp(2,2)$. For this, we use the general coordinate for introducing $\zeta \in SU(2) \sim S^3$:

$$\begin{cases} \zeta_1 = sin\,\alpha\, sin\,\theta\, cos\,\phi \\ \zeta_2 = sin\,\alpha\, sin\,\theta\, sin\,\phi \\ \zeta_3 = sin\,\alpha\, cos\,\theta \\ \zeta_0 = cos\,\alpha \end{cases} \quad (24)$$

where $0 \le \alpha, \theta \le \pi$ and $0 \le \phi < 2\pi$. For every one-parameter subgroup and $(\alpha', \theta', \phi') = g(t).(\alpha, \theta, \phi)$, we can introduce the infinitesimal generator Υ as:

$$\begin{aligned} \left.\frac{\partial[\ell^{\tau}(g)F(\alpha,\theta,\phi)}{\partial t}\right|_{t=0} &= \left.\frac{\partial[(\chi(\zeta,g))^{-2\tau}]}{\partial t}\right|_{t=0} F(\alpha,\theta,\phi) \\ &\quad + (\chi(\zeta,g))^{-2\tau}|_{t=0} \left.\frac{\partial F(\alpha',\theta',\phi')}{\partial t}\right|_{t=0} \\ &= \left[\left.\frac{\partial[(\chi(\zeta,g))^{-2\tau}]}{\partial t}\right|_{t=0} + \left.\frac{\partial\alpha'}{\partial t}\right|_{t=0}\frac{\partial}{\partial\alpha}\right. \\ &\quad \left. + \left.\frac{\partial\theta'}{\partial t}\right|_{t=0}\frac{\partial}{\partial\theta} + \left.\frac{\partial\phi'}{\partial t}\right|_{t=0}\frac{\partial}{\partial\phi}\right] F(\alpha,\theta,\phi) \\ &= -i\Upsilon F(\alpha,\theta,\phi) \end{aligned}$$

$$\begin{aligned} \Rightarrow \Upsilon = i\Bigg(&\left.\frac{\partial[(\chi(\zeta,g))^{-2\tau}]}{\partial t}\right|_{t=0} + \left.\frac{\partial\alpha'}{\partial t}\right|_{t=0}\frac{\partial}{\partial\alpha} + \left.\frac{\partial\theta'}{\partial t}\right|_{t=0}\frac{\partial}{\partial\theta} \\ &+ \left.\frac{\partial\phi'}{\partial t}\right|_{t=0}\frac{\partial}{\partial\phi}\Bigg). \end{aligned} \quad (25)$$

From this later equation and Eqs (14) - (17), we can obtain ten infinitesimal generators on 1+3-de Sitter space.

Calculations of one of the generators (calculations of other similar generators) are brought in Appendix A.

I) Infinitesimal generators of space translation (P)

We derive the infinitesimal generators of space translation from Eq. (14) and (25). This generator is the momentum generator that has vector properties

$$\begin{aligned} P_1 = -i\Bigg(&sin\,\theta\, cos\,\phi\frac{\partial}{\partial\alpha} + cot\,\alpha\, cos\,\theta\, cos\,\phi\frac{\partial}{\partial\theta} \\ &- \frac{cot\,\alpha\, sin\,\phi}{sin\,\theta}\frac{\partial}{\partial\phi}\Bigg), \end{aligned}$$

$$\begin{aligned} P_2 = -i\Bigg(&sin\,\theta\, sin\,\phi\frac{\partial}{\partial\alpha} + cot\,\alpha\, cos\,\theta\, sin\,\phi\frac{\partial}{\partial\theta} \\ &+ \frac{cot\,\alpha\, cos\,\phi}{sin\,\theta}\frac{\partial}{\partial\phi}\Bigg), \end{aligned}$$

$$P_3 = -i\left(cos\,\theta\frac{\partial}{\partial\alpha} - cot\,\alpha\, sin\,\theta\frac{\partial}{\partial\theta}\right).$$

II) Infinitesimal generator of time translation (T)

This generator has the scalar properties (see appendix)

$$T = i\left(\tau \cos\alpha + \sin\alpha \frac{\partial}{\partial\alpha}\right).$$

III) Infinitesimal generators of space rotation (J)

We can obtain this generator from Eqs (16) and (25). It is the angular momentum generator that has the vector properties

$$J_1 = i\left(\sin\phi \frac{\partial}{\partial\theta} + \cot\theta \cos\phi \frac{\partial}{\partial\phi}\right),$$

$$J_2 = i\left(-\cos\phi \frac{\partial}{\partial\theta} + \cot\theta \sin\phi \frac{\partial}{\partial\phi}\right),$$

$$J_3 = i\left(-\frac{\partial}{\partial\phi}\right).$$

IV) Infinitesimal generators of Lorentz boosts (K)

This generator has the vector properties obtained from Eqs (17) and (25)

$$K_1 = i\left(\tau \sin\alpha \sin\theta \cos\phi - \cos\alpha \sin\theta \cos\phi \frac{\partial}{\partial\alpha} - \frac{\cos\theta \cos\phi}{\sin\alpha}\frac{\partial}{\partial\theta} + \frac{\sin\phi}{\sin\alpha \sin\theta}\frac{\partial}{\partial\phi}\right),$$

$$K_2 = i\left(\tau \sin\alpha \sin\theta \sin\phi - \cos\alpha \sin\theta \sin\phi \frac{\partial}{\partial\alpha} - \frac{\cos\theta \sin\phi}{\sin\alpha}\frac{\partial}{\partial\theta} - \frac{\cos\phi}{\sin\alpha \sin\theta}\frac{\partial}{\partial\phi}\right),$$

$$K_3 = i\left(\tau \sin\alpha \cos\theta - \cos\alpha \cos\theta \frac{\partial}{\partial\alpha} + \frac{\sin\theta}{\sin\alpha}\frac{\partial}{\partial\theta}\right).$$

5 Commutation relations of infinitesimal generators

In the previous section, we introduced all of the ten infinitesimal generators on 1+3-de Sitter space. We can directly obtain the associated commutation relations as:

$$[J_i, T] = 0, \tag{26}$$

$$[J_i, J_j] = i\varepsilon_{ijk}J_k, \tag{27}$$

$$[J_i, P_j] = i\varepsilon_{ijk}P_k, \tag{28}$$

$$[J_i, K_j] = i\varepsilon_{ijk}K_k, \tag{29}$$

$$[P_i, P_j] = i\varepsilon_{ijk}J_k, \tag{30}$$

$$[P_i, K_j] = -i\delta_{ij}T, \tag{31}$$

$$[K_i, K_j] = -i\varepsilon_{ijk}J_k, \tag{32}$$

$$[T, P_j] = -iK_j, \tag{33}$$

$$[T, K_j] = -iP_j. \tag{34}$$

To verify the above relations, we profit the Bacry-Levey-leblond (BL) method. Based on BL method, the effect of parity and time reversal operators (Π and Θ) on infinitesimal generators is given by [8]:

$$\Pi: \{T \to T, P \to -P, J \to J, K \to -K\}, \tag{35}$$

$$\Theta: \{T \to -T, P \to P, J \to J, K \to -K\}. \tag{36}$$

If we apply parity and time reversal operators on the left side of Eqs (26) to (34), we can guess the right side of these equations.
For example, we consider the left side of Eq. (32), i.e. $[K_i, K_j]$. From relations (35) and (36) we have

$$\Pi[K_i, K_j] = [\Pi K_i, \Pi K_j] = [-K_i, -K_j] = [K_i, K_j],$$

$$\Theta[K_i, K_j] = [\Theta K_i, \Theta K_j] = [-K_i, -K_j] = [K_i, K_j].$$

In other words, the relation $[K_i, K_j]$ does not change under parity and time reversal operators. According to relations (35) and (36), the only generator not changing under parity and time reversal operators is the generator J. This means that the right side of the relation $[K_i, K_j]$ must be a component of the generator J up to a constant factor (see Eq. (32)).

6 Conclusion

In this work, we studied the ten-parameter de Sitter group. Using the Lorentz space-time decomposition, we introduced ten one-parameter subgroups (or equivalently ten algebraic bases) and ten infinitesimal generators on 1+3-de Sitter space-time. Then, we obtained the commutation relations between these infinitesimal generators. Finally, using the Bacry-Levey-Leblond method, we verified the correctness of one of the commutation relations.

Appendix A: Calculation of infinitesimal generator of time translation

From Eq. (15) we obtain:

$$g^{-1} = \Theta^{-1} = \begin{pmatrix} a' & b' \\ c' & d' \end{pmatrix} = \begin{pmatrix} cosh(\frac{t}{2}) & -sinh(\frac{t}{2}) \\ -sinh(\frac{t}{2}) & cosh(\frac{t}{2}) \end{pmatrix}. \quad (A.1)$$

By choosing ζ as a quaternion, i.e.

$$\zeta = (\zeta_0, \vec{\zeta}) = \zeta_0 + \zeta_1 e_1 + \zeta_2 e_2 + \zeta_3 e_3, \quad (A.2)$$

where $\zeta_0, \zeta_1, \zeta_2, \zeta_3$ are given in Eq. (24), we can write:

$$\chi(\zeta, g) = \chi(\zeta, \Theta) = det(c'\zeta + d') = (cosh\, t - sinh\, t\, cos\, \alpha)^{\frac{1}{2}}, \quad (A.3)$$

$$g^{-1}.\zeta = \Theta^{-1}.\zeta = (a'\zeta + b')(c'\zeta + d')^{-1} = \frac{(cosh\, t\, cos\, \alpha - sinh\, t\, , \vec{\zeta})}{cosh\, t - sinh\, t\, cos\, \alpha} = (\zeta_0', \vec{\zeta}'). \quad (A.4)$$

From the latter equation, we obtain:

$$\zeta_0' = cos\, \alpha' = \frac{cosh\, t\, cos\, \alpha - sinh\, t}{cosh\, t - sinh\, t\, cos\, \alpha}, \quad (A.5)$$

$$\zeta_1' = sin\, \alpha'\, sin\, \theta'\, cos\, \phi' = \frac{sin\, \alpha\, sin\, \theta\, cos\, \phi}{cosh\, t - sinh\, t\, cos\, \alpha}, \quad (A6)$$

$$\zeta_2' = sin\, \alpha'\, sin\, \theta'\, sin\, \phi' = \frac{sin\, \alpha\, sin\, \theta\, sin\, \phi}{cosh\, t - sinh\, t\, cos\, \alpha}, \quad (A.7)$$

$$\zeta_3' = sin\, \alpha'\, cos\, \theta' = \frac{sin\, \alpha\, cos\, \theta}{cosh\, t - sinh\, t\, cos\, \alpha}. \quad (A.8)$$

Also, from these four equations and Eq. (A.3) we can derive:

$$\left.\frac{\partial \alpha'}{\partial t}\right|_{t=0} = sin\, \alpha, \quad (A.9)$$

$$\left.\frac{\partial \theta'}{\partial t}\right|_{t=0} = 0, \quad (A.10)$$

$$\left.\frac{\partial \phi'}{\partial t}\right|_{t=0} = 0, \quad (A.11)$$

$$\left.\frac{\partial[(\chi(\zeta, g))^{-2\tau}]}{\partial t}\right|_{t=0} = \left.\frac{\partial[(cosh\, t - sinh\, t\, cos\, \alpha)^{-\tau}]}{\partial t}\right|_{t=0} = \tau\, cos\, \alpha. \quad (A.12)$$

Finally, from Eq. (25), we derive the infinitesimal generator of time translation as follows:

$$T = i\left(\tau\, cos\, \alpha + sin\, \alpha \frac{\partial}{\partial \alpha}\right).$$

References

1. S. Weinberg, *Gravitation and Cosmology*: Principles and Applications of 260 the General Theory of Relativity (Wiley, New York, 1972)
2. L. Amendola, S. Tsujikawa, *Dark energy theory and observations* (Cambridge University Press, New York, 2010)
3. P. J. E. Peebles, B. Ratra, Rev. Modern Phy. **75**, 2, (2003). J. M. Smith, *Molecular Dynamics* (Springer, Berlin, Heidelberg, 1987)
4. N. Aghanim, Planck Collaboration, Planck 2018 results. VI. Cosmological parameters, 2018, arXiv:1807.06209.
5. A.Rabeie, Eur. Phys. J. C, **72** (2012)
6. A.W. Knapp, *Representation Theory of Semi-simple Groups* (Princeton, NJ: Princeton University Press, 1986)
7. R. Takahashi, Bull. Soc. Math. **91** (1963).
8. H. Bacry, J. M. Levey-Leblond, J. Math. Phys. **9** (1968)

TTMP vol 1(3), 2024
doi: 10.30511/TTMP.2024.2037045.1035

Transactions in Theoretical
and Mathematical Physics

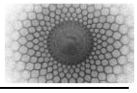

Green's function for a Casimir problem in curved spacetime

Borzoo Nazari[a]

[1]Department of Geodesy, College of Engineering, University of Tehran, Tehran, Iran

Received: 29 July 2024 / Accepted: 14 August 2024 / Published : 16 August 2024

Abstract Obtaining Green's function for problems in curved spacetime is quite important. An important reason is based on the fact that the energy-momentum tensor can be directly calculated from Green's function. The author has found the energy-momentum tensor of the Casimir effect of two plates for a general static spacetime. The process of finding Green's function is discussed here through an introductory manner.

1 Introduction

In curved spacetime, due to the lack of global symmetries, the energy-momentum tensor is very important as a local quantity. Although in some space-times with maximum symmetry such as de Sitter, certain interpretations can be placed on physical quantities, finally, except for some definitions related to the measurement of the number of particles, temperature and the energy-momentum tensor itself, we don't have any other tools to investigate them [1]. Meanwhile, approximate methods in weak spacetimes, as examples close to flat space, are very important. In general, Green's functions are directly, and more easily, related to the energy-momentum tensor through the method of separation of points and reduce the calculations significantly [2]. For weak spacetimes, it is easier to explicitly calculate the Green's function [3] and, in this article, we intend to find an example of it for Casimir plates in a weak spacetime by using elementary methods and without using iterative methods frequently used in the literature. In a way, it can be developed for the strong field as well, which we will mention in the future.

[a]e-mail: borzoo.nazari@ut.ac.ir

2 History of Green's function calculation in the subject

The Green's function for a field theory in the presence of a material boundary is less explicitly calculated. Ref. [4] lists some of these efforts. In general, the attempts made to explicitly calculate the energy-momentum tensor in the Casimir effect are very few. On the other hand, many of implicit results have been investigated [5] and until the author's researches, only in weak spacetime.

$$ds^2 = (1+2\frac{g}{c^2}z)dt^2 - dx^2 - dy^2 - dz^2 \tag{1}$$

sufficient investigations had been done. If $\frac{g}{c^2} \ll 1$, this spacetime will be nothing but accelerated Rindler coordinates in flat spacetime [6]. The metric in accelerated Rindler coordinates can be expressed as

$$ds^2 = (1+\frac{g}{c^2}z)^2dt^2 - dx^2 - dy^2 - dz^2 \tag{2}$$

whose first-order approximation gives (1). It can be said that the momentum-energy tensor for the two parallel plates Casimir effect has not been calculated so far in curved spacetime. The author has completely solved such a problem for an arbitrary static space-time up to the second-order approximation, which is currently under review [7]. In this article, we will discuss in more detail the part related to how to find the Green's function for it.

3 Some basic theorems

Although the following theorems are available in the basic textbooks, their application can create ambiguities. In this section, we emphasize their main aspects. The proof of the following theorems are in ref. [8]

Theorem 1:
The equation

$$a_0(x)y''(x)+a_1(x)y'(x)+a_2(x)y(x)=0, \tag{3}$$

on the closed interval $[a,b]$ under boundary conditions

$$\alpha_1 y(a)=\alpha_2 y'(a),\ \ \beta_1 y(b)=\beta_2 y'(b), \tag{4}$$

where α_1, α_2, β_1 and β_2 are fixed numbers. We consider the function $g(x,s)$ to be a Green's function for the above differential equation with the following conditions [5]:

a) The function $g(x,s)$ solves Eq. (1) for $s\neq x$ in the intervals $a\leq x<s$ and $s<x\leq b$.

b) The function $g(x,s)$ in the interval $a\leq s\leq b$ satisfies the boundary conditions (4).

c) $g(x,s)$ is a continuous function with respect to x and s.

d) The function $\frac{\partial g}{\partial x}$ is continuous in the interval $a\leq x\leq b$, but in $x=s$ has a jump as follows:

$$\frac{\partial g}{\partial x}|_{x=s^+}-\frac{\partial g}{\partial x}|_{x=s^-}=-\frac{1}{a_0(x)}, \tag{5}$$

Theorem 2:
Green's function of Eq.(3) under boundary conditions (4) can be found as follows:

$$G(z,\acute{z})=\begin{cases}\dfrac{Y_1(z)Y_2(\acute{z})}{W(\acute{z})p_0(\acute{z})} & z<\acute{z}, \quad (6a)\\ \dfrac{Y_1(\acute{z})Y_2(z)}{W(\acute{z})p_0(\acute{z})} & \acute{z}<z, \quad (6b)\end{cases}$$

Theorem 3:
The unique answer of the inhomogeneous differential equation

$$a_0(x)y''(x)+a_1(x)y'(x)+a_2(x)y(x)=f(x), \tag{7}$$

in the closed interval [a,b] and under conditions (7) is given by

$$y(x)=-\int_a^b g(x,x')f(x)dx, \tag{8}$$

where $g(x,x')$ is the Green's function of the homogeneous Eq. (8) and $w(s)$ is the Wronskian of two independent solutions $y_1(x)$ and $y_2(x)$ that satisfy the following conditions:

$$\alpha_1 y_2(a)=\alpha_2 y_2'(a),\ \ \beta_1 y_1(b)=\beta_2 y_1'(b), \tag{9}$$

Theorem 4:
If the operator L_x is self-adjoint, then in the differential equation

$$L_x g(x,x')=\delta(x-x'), \tag{10}$$

The function $g(x,x')$ is the same Green's function of Theorem 1 and will be symmetric.

Now we use the above theorems to find the Green's function of the Klein-Gordon equation.

4 Green's function for Casimir effect of parallel plates

Let's assume that two parallel neutral conducting plates are placed near each other and the assembly is placed in a gravitational field. The distance between the plates is a and the metric describes the gravitational field as

$$\begin{aligned}ds^2=&(1+2\gamma_0+2\lambda_0 z)dt^2\\ &-(1+2\gamma_1+2\lambda_1 z)(dx^2+dy^2+dz^2),\end{aligned} \tag{11}$$

where $\lambda_0 z,\lambda_1 z\ll 1$ and $\gamma_0,\gamma_1\ll 1$. The quantum field in the space between the plates is a scalar field satisfying the Klein-Gordon equation

$$\square G_F(x,x')=-\frac{1}{\sqrt{-g}}\delta(x,x'), \tag{12}$$

where

$$\square=\frac{1}{\sqrt{-g}}\partial_\mu(\sqrt{-g}g^{\mu\nu}\partial_\nu)G_F(x,x'), \tag{13}$$

is the Green's function, which is the Feynman propagator. Looking at (11) and (13), we can write the Klein-Gordon equation as follows:

$$\begin{aligned}&\sqrt{-g}g^{11}\partial_z^2 G_F+\partial_z(\sqrt{-g}g^{11})\partial_z G_F\\ &\qquad-\sqrt{-g}g^{11}(k_\perp^2+\frac{g_{11}}{g_{00}}\omega^2)G_F=0,\quad x\neq x',\end{aligned} \tag{14}$$

The condition for the above equation to be self-adjoint is that the coefficient behind $\partial_z G_F$ i.e. $\partial_z(\sqrt{-g}g^{11})$ is the derivative of the coefficient behind $\partial_z^2 G_F$ i.e. $\sqrt{-g}g^{11}$ which is true for the Klein-Gordon equation. Therefore, the obtained Green's function must be symmetrical, and when checking the correctness of the calculations, the symmetry of the obtained Green's function can always be kept in mind. The relation (14) above can be expanded for the metric (11) and by keeping the second order terms in terms of the parameters $\lambda_0 z,\lambda_1 z\ll 1$ and $\gamma_0,\gamma_1\ll 1$ as

$$y''(z)+(\lambda_0+\lambda_1)y'(z)+(a+bz)y(z)=0, \tag{15}$$

where in it we have

$$\begin{aligned}&a=-2B\omega^2, b=(1-2A)\omega^2-k_\perp^2,\\ &A=\gamma_0-\gamma_1,\ B=\lambda_0-\lambda_1,\ \lambda\equiv\lambda_1+\lambda_0.\end{aligned} \tag{16}$$

We note that we have considered the function G_F as the Fourier transform of the function $g_F(z,z')$. The independent answers of Eq. (15) are the same functions $y_1(x)$ and $y_2(x)$ in Theorem 2. These answers have already been found for another purpose in reference [6] and are as follows:

$$Y(z)=D_0(1-(\frac{\lambda}{2}+\frac{a}{4b})z)\sin(\sqrt{b}z(1+\frac{a}{4b}z)+\Theta_0), \tag{17}$$

By setting Θ_0 through applying the boundary condition (Dirichlet), two independent linear responses can be extracted from

it. After doing that, we reach the following results for the Dirichlet boundary condition:

$$y_1(z) = (1-(\frac{\lambda}{2}+\frac{a}{4b})z)\sin\sqrt{b}(z+\frac{a}{4b}z^2) \qquad z<z',$$
$$y_2(z) = (1-(\frac{\lambda}{2}+\frac{a}{4b})z)\sin\sqrt{b}((z-l) + \frac{a}{4b}(z^2-l^2)), \tag{18}$$

As can be seen, according to theorem 3 (see Eq. (9)), the response y_1 at $z=0$ and the response y_2 at $z=l$ become zero. The Wronskian of these two answers is approximated to the second order as follows [4]:

$$W(z^{'}) = (1-\lambda z^{'})\sqrt{b}\sin(\sqrt{b}(l+\frac{a}{4b}l^2)). \tag{19}$$

Putting the above items aside and using Theorem 2, we get after some calculation for $z<z'$,

$$g_F(z,z^{'}) = \frac{1-\gamma_0-\gamma_1-\lambda(z+z^{'})}{2\sqrt{b}\sin(\sqrt{b}(l+\frac{a}{4b}l^2))}(\cos(\sqrt{b}\alpha)-\cos(\sqrt{b})\beta) + \frac{a}{4\sqrt{b}}(z^2-z^{'2}+l^2)\sin(\sqrt{b}\beta) - \frac{a}{4\sqrt{b}}(z^2+z^{'2}-l^2)\sin(\sqrt{b}\alpha),$$

and for $z>z^{'}$ we find

$$g_F(z,z^{'}) = \frac{1-\gamma_0-\gamma_1-\lambda(z+z^{'})}{2\sqrt{b}\sin(\sqrt{b}(l+\frac{a}{4b}l^2))}(\cos(\sqrt{b}\alpha) - \cos(\sqrt{b})(\Delta z-l)) + \frac{a}{4\sqrt{b}}(z^2-z^{'2}-l^2)\sin(\sqrt{b}(\Delta z-l)) - \frac{a}{4\sqrt{b}}(z^2+z^{'2}-l^2)\sin(\sqrt{b}\alpha)), \tag{20}$$

where in it $\alpha = z+z^{'}-l, \beta = z-z^{'}+l = \Delta z+l$. Acoording to theorem 4 the Green function should be symmetric which can be seen from Eqs. (4) and (20). In fact, if one impose the interchange $z \leftrightarrow z^{'}$ to Eq. (4), then Eq. (20) is obtained and vice versa. The point that should be noted is that Eq. (15) is not self-adjoint. This issue is not important because this equation, which is a first-order approximation of the Klein-Gordon equation, has the same answers as Eq. (14).

5 Conclusion

Using preliminary methods, we found the Green's function for the Casimir effect of two parallel conducting plates in a static field described by (11) and showed that it satisfies the Dirichlet boundary conditions on the scalar field in which the Casimir plates are immersed. The metric (11) is actually the extension of an arbitrary static metric in the space between the plates provided that the distance between the plates (denoted by a) is a small value. This distance due to the Casimir effect is usually small and the mentioned condition is fulfilled. On the other hand, if the gravity field is weak by itself, there is no need for a to be small, and the metric (11) can still be considered as a representative of an arbitrary static field. The obtained Green's function in (4) and (20) is very important for calculating the energy-momentum tensor of the problem.

6 Acknowlegnment

The author thanks University of Tehran for supporting this article.

References

1. N.D. Birrell, P. C. W. Davies, *Quantum fields in curved spacetime* (Cambridge University Press, 1982)
2. S.A. Fulling, *Aspects of Quantum Field Theory in Curved Spacetime* (Cambridge University Press, 1989)
3. B. Nazari, Eur. Phys. J. C, **75** (2015)
4. G. Bimonte, E. Calloni, G. Esposito, L. Rosa, Phys. Rev. D, **74** (2006); Erratum ibid. D **75** (2007); Erratum ibid. D **77** (2008); G. Bimonte, G. Esposito, L. Rosa, Phys. Rev. D **78** (2008); G. Bimonte, E. Calloni, G. Esposito, L. Rosa, Phys. Rev. D **76** (2007); G. Esposito, G. M. Napolitano, L. Rosa, Phys.Rev.D **77** (2008); G. M. Napolitano, G. Esposito, L. Rosa, Phys.Rev.D **78** (2008)
5. L.P. Teo, JHEP, **10** (2010); P. Wongjun, Eur. Phys. J. C, **75** (2015); J. Lorenzen, D. Martelli, JHEP, **07** (2015); A. Edery, V. Marachevsky, JHEP, **12** (2008); A. A. Saharian, Phys. Rev. D **69** (2004); A. A. Saharian, Int. J. Mod. Phys. A, **26**, (2011)
6. G. Bimonte, G. Esposito, L. Rosa, Phys. Rev. D **78**, (2008)
7. B. Nazari, Vacuum stress between conducting plates: the curved spacetime version, under review in Phys. Rev. D
8. C.R. Wylie, L.C. Baryet, *Advanced Engineering Mathematics*, (9th Edition, McGrewHill, 1995)
9. B. Nazari, Class. Quantum Grav. **37**, (2020)

TTMP vol 1(3), 2024
doi: 10.30511/TTMP.2024.2035668.1028

Transactions in Theoretical and Mathematical Physics

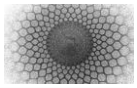

Pair correlation function and its role in characterizing a system of randomly dispersed particles

Hamid Ghorbani[a]

Faculty of Mathematical Sciences, University of Kashan, Kashan, Iran

Received: 14 July 2024 / Accepted: 16 August 2024 / Published: 16 August 2024

Abstract The pair correlation function (or p.c.f.) is a statistical mechanical tool that quantifies the density variation as a function of distance from a reference particle in a system of randomly dispersed particles and is usually used to describe quantitatively, for example, the internal structure of fluids. In this paper, after recalling the p.c.f function to study the interaction behaviour between particles, i.e., attraction, repulsion, or independence, different particle systems are simulated in 2D, and the estimated p.c.fs are interpreted.

Keywords: pair correlation function, inhibition, spatial point process, completely spatial randomness, statistical mechanics, system of particles, intensity.

1 Introduction

In the terminology of spatial point process theory, we say that the centre of a system of randomly distributed particles in 3D is distributed as a spatial point process. Characterizing point processes by their second summary statistic allows us to find out, on average, how the particles interact with each other. Three main classes of interaction behaviour are completely random, inhibition, and attraction. Some authors consider the p.c.f. to be the most important second-order summary of point processes, and it is worth bringing to the attention of scientists willing to use satirical tools to interpret their data. The p.c.f. is not just important, but it is a cornerstone in many subfields of physics. It has been used, for example, in the study of molecular order, fluid dynamics, correlated light scattering, and liquid structures [1].

In the following sections, spatial point processes are first introduced very briefly. Then, the p.c.f. is defined as a second summary statistic for spatial point processes. Its role in characterizing the system of randomly dispersed particles, a crucial aspect of our research, is addressed. Finally, a simulation study improves the paper's readability for researchers working with experimental data.

1.1 A brief review of the spatial point processes theory

Diggle's text comprehensively presents the theory behind point pattern analysis [2]. Data in the form of a set of points irregularly distributed in a region of space arise in many different contexts; examples include the locations of trees in a forest, the locations of cell phone antennas in an urban environment, the centers of pores in a ceramic coating, or the nuclei in a microscopic section of tissue. We call such a data set a spatial point pattern and refer to the locations as events to distinguish them from arbitrary points in the region of interest.

A spatial point process is a stochastic mechanism that generates a countable set of events x_i in the $\mathbb{R}^d$ (in applications d = 2 or 3). A realization of a spatial point process is called to as spatial point pattern and consists of a countable set of points $\{x_1, x_2, \dots, x_{N(A)}\}$ in d-dimensional space. We write N(A) for the number of events in a region $A \subset \mathbb{R}^d, N(A) = \#(x_i \in A)$. We usually deal with processes that are homogeneous (or stationary) and isotropic. A homogeneous process is the one whose distribution is invariant under translation; that is, for an integer k and regions $A_1, A_2, ..., A_k$, the joint distribution of $N(A_1), \dots, N(A_k)$ is equal to the joint distribution of $N(A_1 + \boldsymbol{y}), \dots, N(A_k + \boldsymbol{y})$ for an arbitrary vector $\boldsymbol{y}$. An isotropic point process is the one whose distribution is invariant under rotation. Fluids (liquids and gases) are spatially homogeneous and isotropic. Thus, the average properties of a fluid are invariant with respect to spatially uniform translations through any vector and with respect to arbitrary rotations about any axis [3]. An example of a homogeneous and isotropic point process is the spatial Poisson process, as a model for an ideal gas, referred to as complete spatial randomness (CSR), which is characterized by the following properties

[a]e-mail: hamidghorbani@kashanu.ac.ir

- The number of events in each region A,$N(A)$, follows a Poisson distribution with mean $\lambda.|A|$, where, $|.|$ denotes the area or volume in 2D or 3D, respectively.
- Given $N(A) = n$, the locations of the n events in A are uniformly distributed, i.e. there is no interaction between the points.

The parameter λ, is the intensity of the process, which is the average number of points per unit area or volume, depending on the underlying mathematical space.
In the terminology of statistical mechanics, a CSR system is called a "total disorder" or "unrelated" system.
It is worth mentioning here that we have three main classes of spatial point processes.

The homogeneous Poisson process is completely random (uncorrelated), where a random point at any location does not affect the presence or absence of points at other locations. The inhibited (negatively correlated), where the distances between points are typically larger than expected for a CSR pattern of the same intensity, and the clustered (positively correlated), where the distances between points are typically smaller than expected for a CSR pattern of the same intensity.

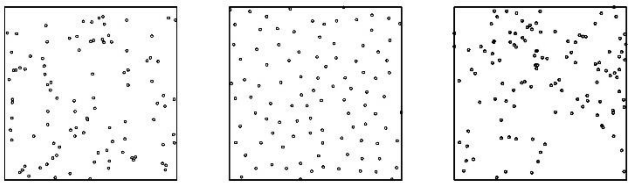

Figure 1 Simulated pattern showing three classes of point processes. From left to right: Poisson, inhibited and attractive patterns. All three patterns are in the unit square.

In other words, when examining the interaction energy of a point pattern at different scales.

The interaction can be attractive or repulsive, depending on geometrical features. The null interaction is associated with the Poisson point process as a reference or benchmark (see Fig. 1).

1.2 Basic Characteristics

Given a spatial point process, let dx and dy denote small regions containing the points x and y, respectively. The (first-order) intensity function is defined as

$$\lambda(x) = \lim_{|dx|\to 0} \frac{E[N(dx)]}{|dx|}. \quad (1)$$

The second-order intensity function is

$$\lambda_2(x,y) = \lim_{|dx|\to 0,|dy|\to 0} \frac{E[N(dx)N(dy)]}{|dx||dy|}. \quad (2)$$

Note that for a homogeneous Poisson process with intensity λ , $\lambda(x) = \lambda, \lambda_2(x,y) = \lambda^2$.

First-order characteristics, such as the intensity function, consider points as individuals, without interaction, while the second-order characteristics consider the interactions between points.

For a homogeneous and isotropic spatial point process, the intensity function is a constant equal to the expected number of events per unit area

$$\lambda(x) = \lambda = \frac{E[N(A)]}{|A|}, \quad (3)$$

and the second-order intensity is reduced to a function of distance:

$$\lambda_2(x,y) = \lambda_2(||x-y||) = \lambda_2(r). \quad (4)$$

The pair correlation function is the normalized second-order intensity function and is defined by:

$$g(x_1,x_2) = \frac{\lambda_2(x_1,x_2)}{\lambda(x_1)\lambda(x_2)}. \quad (5)$$

Again, for a homogeneous and isotropic spatial point process $g(x_1,x_2) = g(||x_1-x_2||) = g(r)$.

The pair correlation function contains information about the short-range correlations. The pair correlation function is a measure that tells us how the density of particles varies as a function of distance from a reference particle. It gives us the probability of finding a particle at a distance from another particle relative to what we would expect if the particles were distributed according to the CSR process. For a CSR process, $g(r) = 1$. If $g(r) > 1$, it means that the particles with distance r are more frequent than in CSR process, which implies that the points tend to cluster relative to a Poisson process with the same intensity function. Similarly, if $g(r) < 1$, the particles with distance r are less frequent than in the CSR process, which implies that the points tend to epel relative to a Poisson process with the same intensity function. The former parenthèse from unity is a measure of the order that becomes less and less present as it increases

2 Importance of the pair correlation function

In a system of randomly dispersed particles, the p.c.f. quantifies how other particles surround the particle of interest. For example, as shown in Fig. 2, the p.c.f. has a constant value at all radial distances for a rarefied gas with no internal structure. In contrast, for a solid system in which molecules are almost uniformly distributed, the pair correlation

function has sharply peaked values at the positions of particles. It is close to zero at the positions where particles are rarely found.

The p.c.f has almost the characteristics of the Dirac delta function for a solid system [5].

The p.c.f. describes the interaction between pairs of particles contained within a given volume. For a homogeneous and isotropically distributed system of particles, the probability of the interaction does not depend on the location or orientation of the particles. In summary, for a system of particles (atoms, molecules, colloids, etc.), the p.c.f. describes how the density varies as a function of distance from

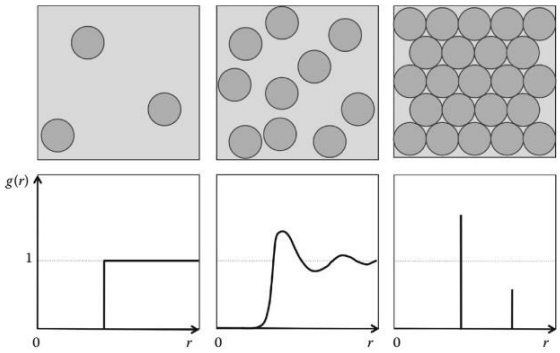

Figure 2 Schematic representation of the p.c.f for different materials. From left to right: liquid, gas and metal [4].

a reference particle. In simple terms, it measures the probability of finding a particle at a given distance of r away from a given reference pparticle relative to that for an ideal gas. Consider that the centers of a system of particles are modelled using a homogeneous isotropic point process with the intensity λ, which is the average number of points per unit volume. The p.c.f $g(r)$ is given by [6]:

$$\lambda^2 g(r) dV_1 dV_2 = P(\text{two points of the process are located in in the infinitesimal volume elements } dV_1 \text{ and } dV_2 \text{ centered in two points at the distance r}) \quad (6)$$

Figs 3, 4 and 5 show the p.c.f. of the point patterns of Fig. 1. The empirical functions (solid lines) deviate from the theoretically expected value in these plots, assuming the points are completely random (dashed lines).

To test whether the deviations in Figs 3,4 and 5 are statistically significant from what we expect under the CSR hypothesis, the standard approach is to use a Monte Carlo test based on envelopes of the p.c.f function obtained from simulated point patterns using the 'spatstat' package in the R statistical software [7]. Fig. 6 shows pointwise 95% confidence bands for the p.c.f. of the Poisson point

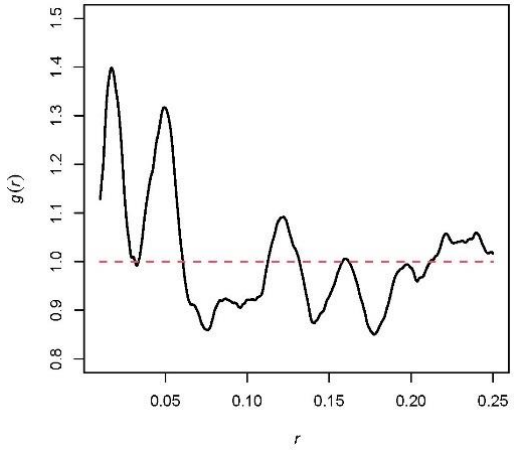

Figure 3: The empirical p.c.f. (solid line) of the Poisson point pattern of Fig. 1.

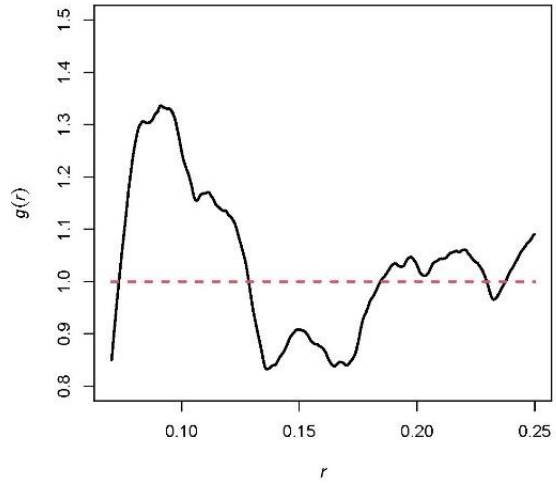

Figure 4: The empirical p.c.f. (solid line) of the repulsive point pattern of Fig. 1.

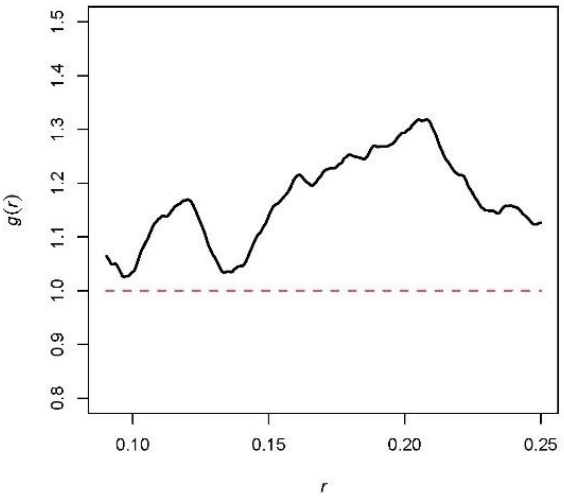

Figure 5: The empirical p.c.f. (solid line) of the attractive point pattern of Fig. 1.

the pattern in Fig.1. Solid lines represent the p.c.f. from Fig. 3. The shading indicates the envelope of values obtained from 199 simulations of complete spatial randomness (CSR). Dashed lines show the theoretical value of CSR. As we see from the figure, the empirical p.c.f. deviations from what we expect under CSR are not statistically significant at the 0.05 level. In Fig. 4, p.c.f. is below the Poisson value, $g(r) < 1$, for distances r up to 0.07 units, then it rises steeply to a value greater than the Poisson value, g(r) > 1 at about r = 0.09 units, before falling back to about 1 for long distances around 0.18. g (r) is zero for r ≤ 0.05, because the regular pattern in Fig. 1, has no interpoint distances shorter than 0.05 units.

Fig. 7 shows the pointwise 95% confidence bands for the p.c.f. of the regular point pattern in Fig. 1. It is clear that for short distances up to r=0.07 we have a negative

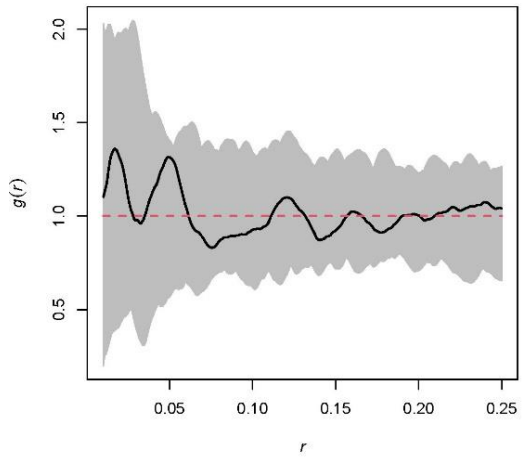

Figure 6: Pointwise 95% confidence bands for the p.c.f. in Fig. 3.

correlation and for r>0.07, the deviation of the empirical p.c.fs from the Poisson theoretical value, is not statistically significant at the 0.05 level.

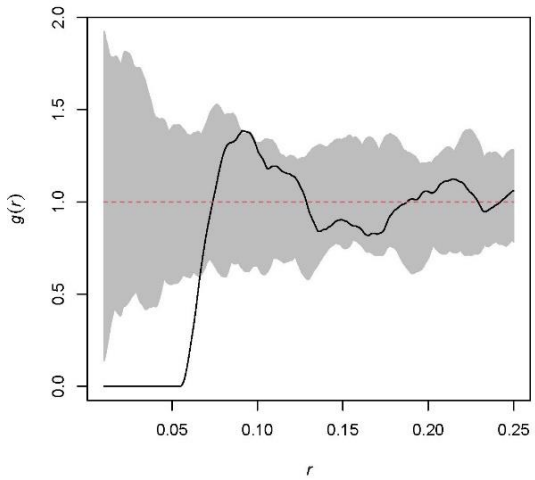

Figure 7: Pointwise 95% confidence bands for the p.c.f. in Fig.4.

Fig. 8 shows pointwise 95% confidence bands for the p.c.f. of the regular point pattern in Fig. 5. Contrary to our expectations, the envelopes here show that the deviations are not significant. By inference, we would say that by looking at the pattern in Fig. 1, the degree of clustering is not observable at any scale compared to what we observe under CSR.

3 Other characteristics defined based on p.c.f.

Two important characteristics, defined based on the p.c.f., are given in what follows.

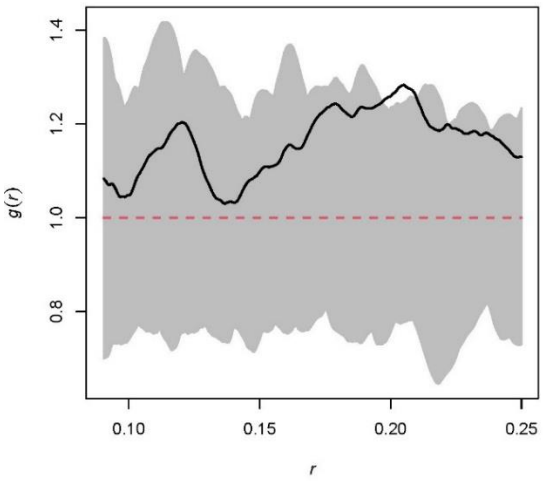

Figure 8: Pointwise 95% confidence bands for the p.c.f. in Fig. 5.

3.1 Radial distribution function

The position r_1 of the first maximum of $g(r)$ gives the average distance of the first nearest neighbors, and its width characterizes the dispersion of the nearest neighbor distances. By definition, the number $dN(r)$ of atoms contained between two concentric shells of radius r and $r + dr$ centered on an atom at the origin is

$$dN(r) = 4\pi\lambda g(r) r^2 dr \tag{7}$$

The radial distribution function (or r.d.f.) is defined as:

$$f(r) = 4\lambda r^2 g(r). \tag{8}$$

3.2 Coordination Number

The r.d.f. is a useful function for counting the number of neighbors by integration. The average number of neighbors around an atom, its coordination number $\bar{N}$, is obtained by

integrating Eq.(7) from 0 to $R = r_{min}$, the first minimum of $g(r)$,

$$\bar{N} = 4\pi\lambda \int_0^{r_{min}} r^2 . \quad (9)$$

Finally, it is worth mentioning that the potential energy [8], [9], the Van Hove pair correlation function, and the Kirkwood-Buff integral [10] are among the other properties defined based on the p.c.f. The Fourier transform of the pair correlation function is called the static structure function S_k. The structure function contains information about the average relative positions of the atoms. Recently, [11] offered an approach based on the pair statistics of disordered particles, simplifying the inverse design of materials with desirable physical and chemical properties.

5. Conclusions

In this paper, we have reviewed the p.c.f., the well-known second summary tool in the theory of spatial point processes, to characterize the density variation as a function of distance from a reference particle in a system of randomly dispersed particles. Although it is defined for 2D and 3D systems of particles, we need a lot of programming skills to compute it in 3D. In the literature, some routines can be implemented for its handling in 3D. For the sake of simplicity, the 2D case has been considered in this paper.

References

1. K. Younge, C. Christenson, A. Bohara, J. Crnkovic, P. Saulnier, Am. J. Phys. **72**, 1247 (2004)
2. P. J. Diggle, *Statistical Analysis of Spatial and Spatio-Temporal Point Patterns* (Chapman & Hall/CRC, Boca Raton, 2014)
3. P. M. Chaikin, T. C. Lubensky, *Principles of Condensed Matter Physics* (Cambridge University Press, London, 1995)
4. N. Kanellopoulos, *Nanoporous Materials: Advanced Techniques for Characterization, Modeling, and Processing* (CRC Press, London, 2011)
5. Z. H Stachurski, *Fundamentals of Amorphous Solids Structure and Properties*. (Wiley-VCH Verlag, Weinheim, 2015)
6. S. N. Chiu, D. Stoyan, W. S. Kendall, J. Mecke, *Stochastic Geometry and Its Applications* (John Wiley and Sons Ltd, New York, 2013)
7. A. Baddeley, E. Rubak, R. Turner, *Spatial Point Patterns: Methodology and Applications with R* (CRC Press, London, 2015)
8. D. Frenkel, S. Berend, *Understanding Molecular Simulation from Algorithms to Applications* (Academic Press, San Diego, 2023)
9. J. D. Poll, S. Miller, J. Chem. Phys. **54** (2013)
10. K. Koga, B. Widom, J. Chem. Phys. **11** (2013)
11. H. Wang, S. Torquato, J. Chem. Phys. **160** (2024)

TTMP vol 1(3), 2024
doi: 1030511/TTMP.2024.2037356.1036

Transactions in Theoretical and Mathematical Physics

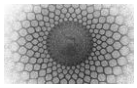

Modeling and investigation of double-layer InP/AlGaInP quantum dot lasers based on dot size*

Mohammad Reza Mansouri[a,1], Tahere Zare[2], Sara Jafakesh[3]

[1] Department of Electrical Engineering, Lamerd Branch, Islamic Azad University, Lamerd, Iran
[2] Department of Mathematics, Beyza Branch, Islamic Azad University, Beyza, Iran
[3] Department of Electrical Engineering, Lamerd Branch, Islamic Azad University, Lamerd, Iran

Received: 02 August 2024 / Accepted: 19 August 2024 / Published: 25 August 2024

Abstract This paper investigates the spectrum theory of a self-aligned InP/AlGaInP bilayer quantum dot laser fabricated by organic-metallic vapour phase epitaxy. The dipole size distribution of quantum dots (groups of small and large quantum dots) has been identified in the fabrication process. Therefore, a model based on song equations that considers the superposition of two heterogeneous groups of quantum dots has been proposed. The total output power and power spectral density (PSD) of the fabricated quantum dot laser at room temperature are determined theoretically. Also, the output spectrum is divided into the sum of two Gaussian (super-Gaussian) curves corresponding to the groups of small and large quantum dots. Each group's peak power spectral density (PSD) and spectral width are extracted, and their dependence on the injection current density is investigated. The results show that the peak corresponding to large quantum dots dominates at low currents, while at high currents, the peak corresponding to small quantum dots dominates, and its spectral width decreases. This behaviour is attributed to the saturation of energy levels of large quantum dots due to their relatively long radiative lifetimes.

1 Introduction

The emergence of quantum dot (QD) lasers in the late 80s marked a revolution in optics and photonics and attracted the attention of scientists in universities and industries. The inherent advantages of these lasers over traditional quantum well lasers have made them ideal options for a wide range of applications. The key feature of many of these lasers that distinguishes them from other lasers is the low threshold current that causes them to require less energy to start operation, resulting in better consumption and higher efficiency [1]. Discrete energy levels cause the electrons to be trapped in these discrete levels and increase the performance and stability of the laser significantly [2]. They work more effectively at higher temperatures than quantum well lasers, making them more suitable for challenging applications and high-pressure environments [3]. Another feature of these lasers is the narrow emission lines that cause them to emit light with a very precise wavelength and produce a purer colour with a broader bandwidth [4]. Significant progress in the growth of self-organizing nanostructures with small sizes is the turning point of these lasers, which enables the production of lasers with arbitrary wavelengths [5]. This spectral performance enables high-bandwidth data transmission with visible light, revolutionizing next-generation communications. Another feature of QD lasers is their higher precision and sensitivity in making optical sensors that can be used in medical, military, and measurement imaging applications. Temperatures are used [6] and are also a key component for the development of quantum computers and other quantum technologies in the future [7]. Red-wavelength quantum dot (QD) lasers made of InP implanted on a GaInP base have a dual dot size distribution (small and large quantum dots) [8]. This effect is related to the roughness angle of the substrate and different growth conditions such as surface diffusion, growth temperature, and growth rate. Due to the limitations of the jump between the barrier band and the energy levels, the expected stability threshold of the laser decreases with increasing temperature. As a result, aluminium (Al) is added to the barrier material to reduce the possibility of thermal escape of charge carriers and, as a result, confinement of point charge carriers. Quantum increases [9]. The amount of aluminium is adjusted according to what was suggested in [10] to reach the optimum composition of InP implanted in the (Al0.1Ga)0.51InP barrier [11]. Although the difference between the ground state and the first excited state is small, 13 nm, the gain is nevertheless limited by the low dot density and poor optical confinement factor. To overcome this challenge, a solution based on the vertical arrangement of QD layers has been proposed, which offers several advantages, including higher gain [12], the possibility of ground state emission, and a higher gain saturation limit [13]. By increasing the number of stacked layers, a shift towards red wavelengths is observed in the laser [14]. In addition, overlapping layers lead to increased external efficiency [15]. In [16], two InP layers in (Al0.1Ga)0.51InP barriers with a spacer thickness of 6 nm have been achieved with a pure mode efficiency of 68.5% compared to 43.7% for a single layer [17], and the change in wavelength between the peaks The two groups of QDs

[a]e-mail: mansouri1902@gmail.com

(small and large) are about 45 nm. Therefore, modelling these important effects using song equations is necessary to fully understand the optical properties of lasers. This paper presents a theoretical model based on experimental data for InP/(Al0.1Ga)0.51InP double-layer quantum dot lasers with a 4 nm spacer fabricated by metal-organic vapor phase epitaxy [18]. The proposed model is based on the song equations and considering the combination of two heterogeneous groups of quantum dots (small and large) that are formed during the construction, the output spectrum is divided into the sum of two Gaussian curves belonging to the small and large QD groups. The peak power spectral density (PSD) and spectral width of each group in the output spectrum are extracted, and their dependence on the injection current density is analyzed. This model is the first model for the binary size distribution of QD InP laser systems. The organization of the structure of this article includes an introduction of the QD multi-mode rate equation model, an experimental model, a discussion about theoretical results, and comparison with the experimental model, and a conclusion.

2 Modeling of the rate equation

This model is based on considering two types of heterogeneity in the system. The first type is the inhomogeneity between small and large groups of quantum dots, which was observed in the atomic force microscope (AFM) images in sources [19] and [20]. The second type is heterogeneity within each group due to size variations around the standard QD size. It is assumed that all quantum dots are spatially separated and the two QD layers do not interfere with each other so that the output of the laser system is the sum of their outputs. The presence of two layers results in a larger number of QDs and, consequently, a higher gain. The neutrality of the QD is maintained by trapping only electron-hole pairs with equal lifetimes. The principle of Pauli exclusion and spin degeneracy is respected in the calculations. The system's operation starts with injecting pulsed current source carriers into the coating layer. The carriers then move to the active region, releasing them from the barrier through the wet layer. Finally, the carriers are trapped at the highest energy level inside each QD and can then escape to lower energy levels. The number of energy levels and their energy separation depends on the QD size. For example, a large QD has multiple energy levels with little energy difference. On the contrary, the small size of the QD leads to a smaller number of energy levels with a greater distance between them. The presented model assumes that all the carriers injected by the pulsed current source reach the wet layer, the lowest energy level, and the ground state inside each QD is considered. The energy level of the wet layer (E2) and the ground state energy levels of the two QD groups are ($E1^S$, and $E1^L$), referring to the small and large groups; the wet layer collects carriers with an average injection rate that is similar to the effective current of the pulsed current source. When the carrier reaches the ground state, carrier-photon interactions occur through the gain-excited process (gm^S, gm^L). The numerical model is based on the solution of the photon-carrier rate equations in the framework of the model of the main equations of carrier dynamics. Fig. 1 shows the proposed model.

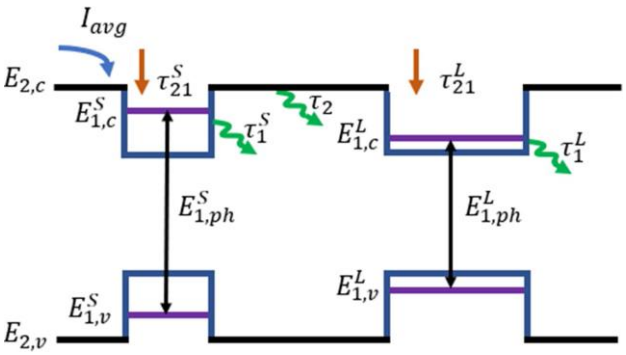

Figure 1 Carrier dynamics model with energy levels and wet layer of quantum dot laser.

The propagation equations of the input signal take an exponential form in each section to amplify the signal through the cavity length, which is as follows. For more details on equations and the introduction of parameters, see [15]. Therefore, the numerical solution of the rate equations with the fourth-order Runge–Kutta method is used in each section for all cavity modes to evaluate the spectrum in the QD laser. rate equations are solved numerically in this section with MATLAB software, and ode45 code was used for this analysis. Some parameters used in the calculations are listed in Tab. 1.

Table 1 Parameters which are used in the calculation and simulation

Parameter	Symbol	Value
Active region length	$[L]$	1200 μm
Active region width	$[W]$	1.50 μm
Band gap	$[Eg]$	0.08eV
Central transition energy of GS	$[Ej]$	0.9493eV
Central transition energy of ES1	$[Em]$	1.0221eV
Number of QDs layers	$[Nl]$	10
Optical confinement factor	$[\Gamma]$	0.1
Carrier recombination lifetimes in dots	$[\tau r]$	1ns
Carrier recombination lifetimes in WL	$[\tau \omega r]$	0.4ns
Temperature	$[T]$	295K

$$\frac{dN_2}{dt} = \frac{I_{avg}}{e} - N_2 \sum_L^{N_L} \frac{(1-f_1^l)G^L}{\tau_{21}^L} - N_2 \sum_S^{N_S} \frac{(1-f_1^S)G^S}{\tau_{21}^S} - \frac{N_2}{\tau_2} + \sum_L^{N_L} \frac{(1-f_2^L)N_1^L}{\tau_{21}^L} + \sum_S^{N_S} \frac{(1-f_1^S)N_1^S}{\tau_{12}^S} \quad (1)$$

$$\frac{dN_1^L}{dt} = \frac{N_2 G^L}{\tau_{21}^L}(1-f_1^L) - \frac{N_1^L}{\tau_1^L} - \frac{(1-f_2^L)N_1^L}{\tau_{12}^L} - \Gamma_L \sum_m^{N_m} g_{m,1}^L v_g S_m \quad (2)$$

$$\frac{dN_1^S}{dt} = \frac{N_2 G^S}{\tau_{21}^S}(1-f_1^S) - \frac{N_1^S}{\tau_1^S} - \frac{(1-f_2^S)N_1^S}{\tau_{12}^S} - \Gamma_S \sum_m^{N_m} g_{m,1}^S v_g S_m \quad (3)$$

$$\frac{dS_m}{dt} = \Gamma_L \sum_L^{N_L} g_{m,1}^L v_g S_m - \Gamma_S \sum_S^{N_S} g_{m,1}^S v_g S_m + \beta_L \sum_L^{N_L} \frac{N_1^L}{\tau_1^L} + \beta_S \sum_S^{N_S} \frac{N_1^S}{\tau_1^S} - \frac{S_m}{\tau_{ph}} \quad (4)$$

τ_{ph} is the photon lifetime in the cavity. The overall optical gain is given by the following equation:

$$g'_{m,L} = \frac{2\pi e^2 \hbar < R_{eh} > N_{QD}^j}{c n_r \varepsilon_o m_o^2} \left(f_{L,c}^j - f_{L,o}^j\right) G^j\left(E_j - E_j^o\right) \times (E_m - E_j) \quad (5)$$

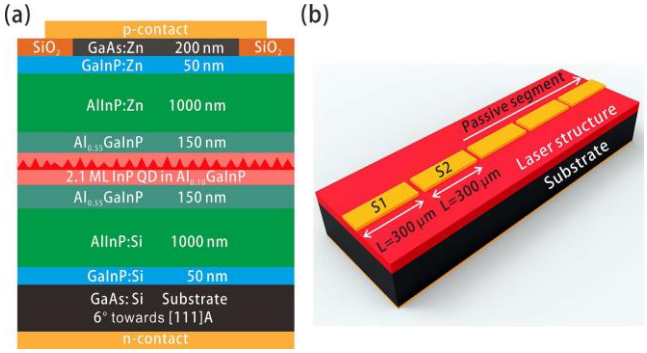

Figure 3 Schematic drawing of the test structures (not to scale): (a) Epitaxial layers designed for a 660 nm emitting InP/AlGaInP QD broad area laser. (b) Measured structure of the optical gain and absorption spectra with segmented contact sections. S1: segment 1, S2: segment 2, Passive segments: the long enough segment sections to avoid the reflected light.

The homogeneous broadening of the induced emission process with the Lorentzian function is given as follows.

$$B_{cv,j}(E_m - E_j) = \frac{\hbar\,\Gamma_{cv,j}/\pi}{(E_m - E_j)^2 + (\hbar\Gamma_{cv,j})^2} \quad (6)$$

$\hbar\Gamma_{cv,j}$ is the FWHM (full width at half maximum) of the homogeneous broadening in each energy state. The inhomogeneous spread with Gaussian distribution function is given below:

$$G^j(E_j - E_j^o) = \frac{1}{\sqrt{2\pi}\varepsilon_o} exp\left[-(E_j - E_j^o)^2/2\xi_o^2\right] \quad (7)$$

3 Experimental model

The investigated QD laser structure was grown by metal-organic vapour-phase epitaxy (MOVPE) on a Si-doped (100)-GaAs substrate with a misorientation of 6^0 toward the $[111]_A$ direction. An AIX-200 horizontal reactor was used for the epitaxial growth with standard precursors (trimethylgallium, trimethylindium, trimethylaluminium, arsine, and phosphine), at a high temperature of 710^0 C and a reactor pressure of 100 mbar to achieve a high density of QDs. As shown in Fig. 2(a), from bottom to top, the laser structure consists of a 100-nm-thick GaAs: Si buffer layer, followed by a 50-nm-thick Ga 0.52 In 0.48 P: Si intermediate layer and a 1000-nm thick Al0.52 In 0.48 P: Si optical confinement layer (OCL). Afterwards, a single sheet of 2.1 monolayers (ML) self-assembled InP QDs were grown in the Stranski-Krastanow (S-K) mode and placed in the centre of the 2 × 10 nm undoped Al0.10 GaInP barriers. The barrier layers were carefully adapted to be lattice-matched to GaAs. The entire active region was surrounded by 2 × 150 nm undoped Al0.55 GaInP waveguide layers to form the separated confinement structure (SCH) and get the highest optical confinement factor in the vertical direction. The p-side has a structure similar to the n-side, while the dopant was changed to zinc. The layers were finally capped by a 200-nm-thick heavily doped GaAs: Zn layer to form an ohmic contact with low resistance. For the processing of broad-area lasers, a 100-µm-wide stripe contact layer of GaAs: Zn was first formed by photolithography and wet chemical etching to reduce the current spreading in the lateral direction. After depositing a SiO_2 insulation layer, Pd/Au layers were metalized on top to form the p contact. To reduce the thermal effect, the substrate was polished down to about 130 µm, followed by depositing the Cr/Au-based n-contact on the substrate backside. Afterwards, the sample was processed into the Fabry-Perot (FP) lasers by cleaving the facets with different cavity lengths between 0.55 and 2.24 mm.

The segmented contact method described in [21] was utilized to measure the optical gain and absorption spectra by analyzing the amplified spontaneous emission (ASE) as a function of the contact stripe length. To implement this method, the p-contact of the gain-tested sample, as represented in Fig. 2(b), was separated into 300-µm-long segments with a gap of 5 µm in between, while the segment width remained 100 µm. All the cleaved facets of the test samples were uncoated. The samples were measured on the brass heatsink controlled by a temperature controller, and the current application was done using an Au-coated tungsten probe. The measurements were operated under the pulsed current driven with a duration of 300 ns and a duty cycle of 0.15% to avoid the self-heating effect.

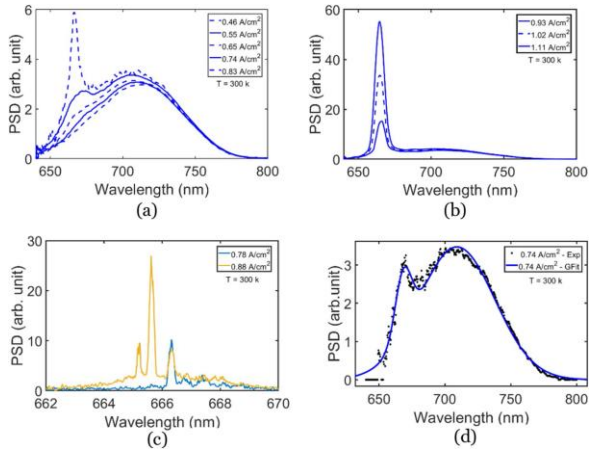

Figure 4 PSD versus wavelength for different current densities.

This section presents the results of the experimental study on the InP/AlGaInP bilayer quantum dot laser chip at room temperature. These results are taken from [15] and [21]. Fig. 3 shows the relationship between the average output power of the InP/AlGaInP bilayer quantum dot laser and the average injected current density for three different duty cycles (0.075%, 0.1% and 0.15%) at room temperature. Fig. 4 shows the laser output spectrum for different average injection current densities and duty cycle of 0.1%. The resolution of the spectrometer analyzer is set to 50 picometers in figs (c4) and 2 nm for the other figures. Also, the information extracted from Gaussian fitting for groups of small and large quantum dots against the average current density is shown in Figs (5a) and (5b). These observations can be explained as follows. In the first region, where large quantum dots dominate the spectrum, the small energy separation of the excited states for the group of quantum dots facilitates carriers' transition from the wet layer to the ground state in a shorter time than for small quantum dots. However, in the second and third regions, as shown in Fig. 3a, small quantum dots dominate and emit lasers, while large quantum dots are saturated. This is due to the higher mode gain of small quantum dots compared to larger dots [22]. Even at low injected current density, the luminescence of large quantum dots saturates, and the overall spectrum shifts to shorter wavelengths (Fig. 4a). This behavior is due to the filling of the ground state due to the weak overlap of wave functions between electrons and holes, which leads to long lifetimes of charge carriers. Charge carriers in small quantum dots show a stronger overlap of wave functions and therefore recombine much faster, leading to Higher emission intensities in higher energy spectral range.

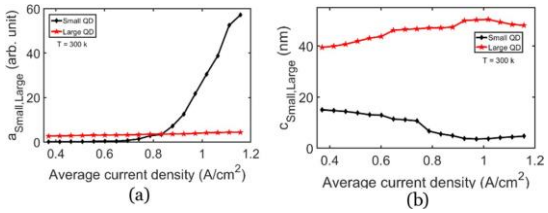

Figure 5 Data extraction for small and large QD groups from Gaussian fitting versus average current density. a. The peak amplitude of the Gaussian PSD. b. Gaussian spectral width.

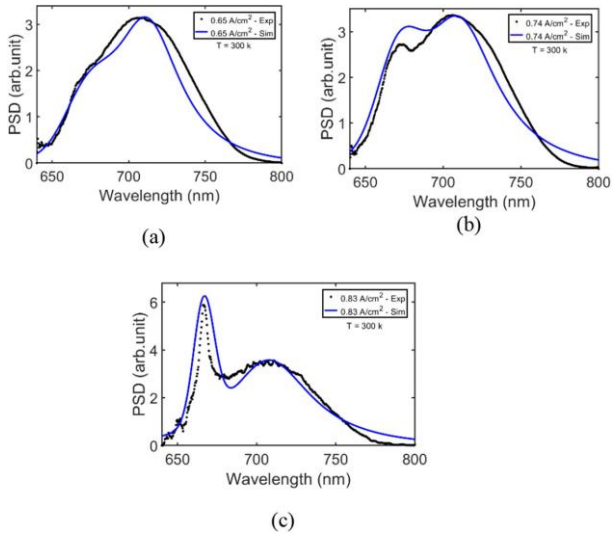

Figure 6 PSD in terms of wavelength for experimental data (dotted black) and simulation results (blue) at three different current densities.

4 Comparison of modeling results with experimental results

Research has shown that smaller quantum dots have only one bound energy level for electrons, while larger quantum dots have at least two levels. This leads to faster trapping times for larger quantum dots with significant ground state filling. As mentioned above, recombination occurs faster in small quantum dots due to stronger overlapping of wave functions, so the radiative lifetime for small quantum dots is set to smaller values than larger dots. Fig. (5) is used for the extracted spectral width and central wavelength values.

Figs (a6) to (c6) show the power spectral density in terms of wavelength obtained from model simulation and experimental data for three different average injection current densities. These figures show the transition between the three regions discussed earlier. The error percentage of the experimental and theoretical results is around 1.5 to 10%. Therefore, a good overall agreement was obtained between the theoretical and experimental results for different mean current densities.

5 Conclusion

This research presented the experimental and theoretical investigation of a double-layer quantum dot laser with the superposition of small and large quantum dots. Also, the dipole size distribution of quantum dots in InP lasers was presented for the first time. We showed that small quantum dots have the greatest effect on laser performance. they had. A two-peak Gaussian fitting model was applied to the data to extract the central emission wavelengths and the percentage contribution of small and large quantum dots in the emission. It is shown that small quantum dots dominate and emit lasers, while large quantum dots saturate. This is due to the higher mode gain of small quantum dots compared to larger dots. The theoretical model described this phenomenon as the superposition of two groups of heterogeneous quantum dots. The simulation results were compared with the experimental data, and the error percentage was obtained in the range of 1.5% to 10%, indicating a good agreement.

References

1. P. R. A. Abbas, H., Omran, Y. M.,Sabry; , 27th Intern. Semiconduct. Laser Conference (2021)
2. M. Asada, Y., Miyamoto, Y. Suematsu, IEEE J. Quantum Electron, **22** (1986)
3. G. J. Beirne, P. Michler, M. Jetter, H. Schweizer, J. Appl. Phys. (2005)
4. S. Breuer, M. Rossetti, L. Drzewietzki, P. Bardella, I. Montrosset, W. Elsaser, IEEE J. Quant. Elect. **47** (2011)
5. M. Califano, P. Harrison, Phys. Rev. B, **61** (2000)
6. N. Dogru, H. S. D. Tunc, et al. Opt. Laser Technol. **148** (2022)
7. J. F. Ehlert, A. Mugnier, G. He, F. GrillotLaser Phys. **31**, 8, (2021)
8. T. Finke, V. Sichkovskyi, J. P. Reithmaier, IEEE Photon. Technol. Lett. **33**, 14 (2021)
9. J. O. Gerguis, Y. M. Sabry, H. Omran, D. J. Khalil, J. Lightwave Technol. **37**, 20 (2019)
10. F. Grillot, K. Veselinov, M. Gioannini, I. Montrosset, J. Even, R. Piron, E. Homeyer, S. Loualiche, Quantum **45**, 7 (2009)
11. S. Grosse, J. Sandmann, G. von Plessen, J. Feldmann, H. Lipsanen, M. Sopanen, J. Tulkki, Phys. Rev. B **55**, 7 (1997)
12. I. S. Han, J. S. Kim, J. C. Shin, J. O. Kim, S. K. Noh, S. J. Lee, S. J. Krishna, Lumin. **207** (2019)
13. Z. Huang, S. Hepp, R. Sittig, M. Jetter, P. Michler, Optics InfoBase Conf. Pap. **140** (2009)
14. Z. Huang, M. Zimmer, S. Hepp, M. Jetter, P. Michler, IEEE J. Quantum Electron. **55**, 2 (2019)
15. S. M. Izadyar, M. Razaghi, A. Hassanzadeh, Opt. Quant. Electron. **50**, 1 (2018)
16. Z.F. Jiang, Z. M. Wu, E. Jayaprasath, W. Y. Yang, C. X. Hu, G. Q. Xia, Photonics **6**, 2 (2019)
17. A. V. Nenashev, A. V. Dvurechenskii, J. Appl. Phys. **10** (2020)
18. A. Quirce, M. Virte, *Nonlinear Dynamics of Semiconductor Lasers and Their Applications* (MDPI-Multidisciplinary Digital Publishing Institute, 2022)
19. J. Wang, F. Sciarrino, A. Laing, M. G. Thompson **14**, 5 (2020).
20. Y. Xiong, X. Zhang, J. Appl. Phys. **125**, 9 (2019)
21. Y. Zhang, L. Wang, K., Wang, K. S. Wong, K. Wu, IEEE Access **7**, 1 (2019).
22. Y. Zhou, J. Duan, F. Grillot, C. Wang, IEEE J. Quant. Electron (2020).

TTMP vol 1(3), 2024
doi: 10.30511/TTMP.2024.2036115,1034

Transactions in Theoretical and Mathematical Physics

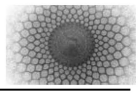

Optical Instabilities in a Media with Quantum Inference Effects in a Micro-Ring Resonator

M.Javad Mohammadpour Nashrudkoli[1,a], M.Reza Poorsadegh bejargafsheh

[1]Department of Physics, University of Guilan, Rasht, Iran

Received: 24 July 2024 / Accepted: 25 August 2024 / Published: 30 August 2024

Abstract We present optical instabilities in a micro-ring resonator filled with media that includes quantum inference effects. The quantum interference effects we consider is a three-level atomic media whose levels are coupled by two laser beams under the Λ-type configuration. Under fast response conditions, we obtain optical instabilities in an all-optical bistable system and study the dynamics of the instability in the regime gain without inversion, which is due to the existence of the Hopf instability in the lower branch of homogeneous stationary state solutions. We also investigated the dynamics of the system under the scan of the control parameter adiabatically, where the temporal oscillations of the intensity are period one, and the phase space of the field is a limit cycle.

1 Introduction

Dynamic behaviour of Optical instability in atom resonator coupled systems has been studied extensively over four decades, particularly in the context of lasers and optical bistability [1–6]. The all-optical bistability (AOB) phenomenon fundamentally affects the cooperative dynamics between atoms and the field. The motivation for the AOB of two-level atoms primarily stems from its prospective applications in all-optical switching, essential for progresses in all-optical communication and computing technologies. Furthermore, AOB elucidates various quantum optical phenomena such as optical instabilities, self oscillations, and chaotic behaviour [7]. Effects of single-mode dynamical instability in a two-level AOB system were first explored in the framework of a plane-wave model. This analysis was subsequently extended to the Gaussian field model addressing its experimental feasibility [8]. Numerous studies have explored the interactions of three-level atomic configuration patterns and multi-mode fields that lead to chaotic behaviour. Savage et al. [9] investigated the possibilities of tri- and quadra-stability alongside the phenomena of self-pulsing and optical turbulence. Similarly, Grangier et al. [10] focused on optical bistability within the dispersive regime and illustrated how chaos can emerge at elevated intensities of the field. Additionally, chaotic behavior has been observed in the Λ configuration pattern of a three-level atomic system where feedback is exclusively applied to the probe field; detuning of the coupling field is employed to induce chaos at higher input intensities [11]. Extensive research has been conducted on cooperative effects and investigating nonlinear dynamical characteristics, including self oscillating and pulsing, instabilities, and chaotic behaviour [12].

The coherent manipulation of quantum states in at-oms and molecules through the coherent light of a laser can give rise to quantum interference in the probability amplitudes of the wave function in transition pathways induced by optical excitation [13]. Quantum interfer-ence and quantum coherence in an atomic system can give rise to numerous significant optical phenomena, such as electromagnetically induced transparency (EIT) [13–16], optical bistability (OB) [17], stimulated Raman adiabatic passage (STIRAP) [18], enhanced index of refraction [19], lasing without inversion [20, 21], etc., were also studied in recent years.

Dynamic of Optical instability, in media that includes quantum inference effects confined in a ring resonator holds substantial theoretical and experimental significance. Investigations on the spatio-temporal dynamics of cavities under such quantum interference effects in 3-level systems began by the Gian-Luca Oppo and were later extended to many important investigations in 2D and 1D [22–26]. These studies considered Λ atomic configuration to realize coherent population trapping and EIT, where many novel phenomena were discovered, yet many other related topics remain to be investigated. However, the nonlinear dynamics of temporal to researchers [27, 28].

[a]e-mail: mj.mohammadpour99@gmail.com

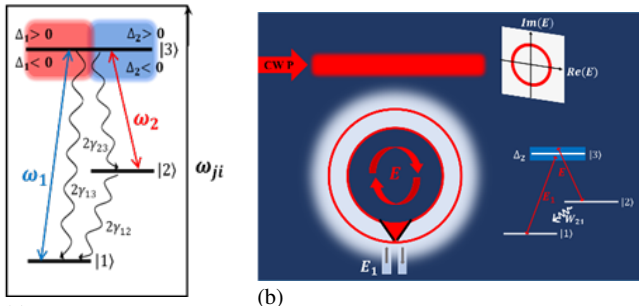

(a) (b)

Figure 1: (a) The Λ coupling pattern of three-level atomic media that interact with the two coherent fields having amplitudes E_1 and E_2 at frequencies ω_1 and ω_2, respectively, and Δ_1 and Δ_2 the respective detuning parameters. (b) A schematic of the micro-ring resonator configuration within pump P and E_1 as input fields, and E as circulating field, filled with media that includes the Λ atomic coupling model with the ground, metastable, and excited states $|1\rangle$, $|2\rangle$, and $|3\rangle$ respectively.

The current study aims to present the instabilities of bistable optical systems in a micro-ring resonator filled with media that includes quantum interference effects. The quantum interference effect we consider is a three-level atomic media whose levels are coupled by two laser beams under the Λ-type coupling pattern. We have identified and explored three regimes of operation depending on the population decay rate of level $|2\rangle$ to level $|1\rangle$ and the ratio of the driving field amplitudes: 1) gain without inversion (this is similar to lasing without inversion), 2) gain with inversion, and 3) inversion without gain. The dynamics of temporal oscillations of the field, which circulates in a resonator, is the focus of our interest. These oscillations arise from the nonlinear reaction of three-level atomic media to the driving fields in the micro-ring resonator in the mean-field limit.

2 Theoretical Model

An alternative promising configuration whose temporal dynamics under the fast response condition in a cavity is not studied is the Λ system, where a single excited upper level (3) is coupled to two lower levels (ground state (1) and meta-stable state (2)). The atomic configuration of interest is shown in Fig. (1.a) and that of the micro-ring resonator containing such medium in Fig. (1.b).

2.1 Interaction Hamiltonian and density matrix

We focus on the Λ coupling pattern of a three level ato-mic system excited by two coherent laser lights with driving frequencies ω_1 and ω_2, as demonstrated in Fig. (1.a). In this study, we employ the semiclassical approach in which the creation and annihilation operators, known as fermion operators, act on an electron at the discrete atomic states. The levels coupled by the driving fields exhibit dipole-allowed transitions; however, the transition from $|1\rangle$ to $|2\rangle$ is dipole-forbidden due to the parity selection rule.

The Hamiltonian that describes the interaction of a three-level atomic configuration, selected from an infinite number of possible levels of an atomic mixed state, with two coherent laser fields treated as classical sources in the rotating-wave approximation, is formulated by appropriately adapting the Hamiltonian of a typical two-level atom-field interaction [29] to the present problem, as follows:

$$\mathscr{H} = \sum_{i=1}^{3} \varepsilon_i a_i^\dagger a_i + \hbar g_1 \left(a_3^\dagger a_1 e^{-i\omega_1 t} + a_1^\dagger a_3 e^{i\omega_1 t} \right) + \hbar g_2 \left(a_3^\dagger a_2 e^{-i\omega_2 t} + a_2^\dagger a_3 e^{i\omega_2 t} \right) \quad (1)$$

Here, ε_i $(i = 1,2,3)$ are the eigenenergies of the discrete atomic states, g_1 and g_2 are the Rabi frequencies of the coupling fields E_1 and E, and $a_i^\dagger = |i\rangle$ and $a_i = \langle i|$ $(i = 1,2,3)$ are electron creation and annihilation operators, respectively.

We note that excitation (de-excitation) of an electron to (from) level $|3\rangle$, corresponding to its creation (removal) in (from) that state, can happen through two routes: $|1\rangle \leftrightarrow |3\rangle$ and $|2\rangle \leftrightarrow |3\rangle$. The full master equation, containing reversible and irreversible parts following the Liouville-von Neumann equation in the interaction picture, can be written as follows:

$$\frac{\partial \rho}{\partial t} = -\frac{i}{\hbar}[\mathscr{H}_I, \rho] + \Lambda\rho, \quad (2)$$

where

$$\mathscr{H}_I = \hbar g_1 \left(a_3^\dagger a_1 e^{-i\Delta_1 t} + a_1^\dagger a_3 e^{i\Delta_1 t} \right) + \hbar g_2 \left(a_3^\dagger a_2 e^{-i\Delta_2 t} + a_2^\dagger a_3 e^{i\Delta_2 t} \right), \quad (3)$$

and the material detunings are defined as $\Delta_1 = \omega_1 - \omega_{31}$ and $\Delta_2 = \omega_2 - \omega_{32}$, with ω_{31} and ω_{32} representing the atomic transition frequencies. Effects of spontaneous emission and complex rate constants are described by Λ_ρ, where the population transition rates between levels i and j are represented by W_{ij} and polarization decay rates by γ_{ij}.

Following the phenomenological approach, and noting that for the three-level case there is more than a single route for a population of a level to change due to spontaneous emission, the density matrix elements, i.e., ρ_{ij} as defined in Eq. (2), contain complex unambiguous time-dependent exponential terms. These can be eliminated using the following transformation:

$$R_{ii} = \rho_{ii} \tag{4a}$$

$$R_{13} = \rho_{13} e^{-i\Delta_1 t} \tag{4b}$$

$$R_{23} = \rho_{23} e^{-i\Delta_2 t} \tag{4c}$$

$$R_{12} = \rho_{12} e^{-i(\Delta_1 - \Delta_2) t} \tag{4d}$$

where R_{ij} denotes the transformed elements of the equation of motion. This simplification significantly improves our capacity to analyze and interpret the behavior of the system. It should be observed that damping rates for coherence terms follow the relation

$$\gamma_{ij} = \frac{1}{2} \sum_k \left(W_{ik} + W_{jk} \right), \tag{5}$$

where the downward population decay rates W_{ij} (with $i > j$) describe the spontaneous decay rate of the excited state. In contrast, excitations from a stable and metastable state to an excited state due to collisional processes have been effectively disregarded, as the energy separations between the levels are significantly greater than kT [30]. Based on this, we arrive at the following expressions:

$$\gamma_{12} = \frac{1}{2} \left(W_{12} + W_{13} + W_{21} + W_{23} \right) \approx \frac{W_{21}}{2}, \tag{6}$$

$$\gamma_{13} = \frac{1}{2} \left(W_{12} + W_{13} + W_{31} + W_{32} \right) \approx \frac{W_{31} + W_{32}}{2}, \tag{7}$$

$$\begin{aligned} \gamma_{23} &= \frac{1}{2} \left(W_{21} + W_{23} + W_{31} + W_{32} \right) \\ &\approx \frac{W_{21} + W_{31} + W_{32}}{2}, \end{aligned} \tag{8}$$

$$\Psi = \left(\alpha_{12} \cdot \beta_{12} \cdot \alpha_{13} \cdot \beta_{13} \cdot \alpha_{23} \cdot \beta_{23} \cdot R_{22} \cdot R_{33} \right)^T, \tag{9}$$

Eq. (2) leads to 8 linear time-independent equations for the transformed elements of the equation of motion R_{ij} in the form of $\partial_t \Psi = M\Psi + I$. At steady state, we have:

$$(-2g_2)\beta_{23} - W_{21}R_{22} + W_{32}R_{33} = 0, \tag{10.a}$$

$$(2g_1)\beta_{13} + (2g_2)\beta_{23} - (W_{31} + W_{32})R_{33} = 0, \tag{10.b}$$

$$(\Delta_1 - \Delta_2)\alpha_{12} + \gamma_{12}\beta_{12} - g_2\alpha_{13} + g_1\alpha_{23} = 0, \tag{10.c}$$

$$\gamma_{12}\alpha_{12} + (\Delta_2 - \Delta_1)\beta_{12} + g_2\beta_{13} + g_1\beta_{23} = 0, \tag{10.d}$$

$$g_2\beta_{12} + \gamma_{13}\alpha_{13} - \Delta_1\beta_{13} = 0, \tag{10.e}$$

$$-g_2\alpha_{12} + \Delta_1\alpha_{13} + \gamma_{13}\beta_{13} + g_1R_{22} + 2g_1R_{33} = g_1, \tag{10.f}$$

$$g_1\beta_{12} - \gamma_{23}\alpha_{23} + \Delta_2\beta_{23} = 0, \tag{10.g}$$

$$g_1\alpha_{12} - \Delta_2\alpha_{23} - \gamma_{23}\beta_{23} + g_2R_{22} - g_2R_{33} = 0, \tag{10.h}$$

where α_{ij} and β_{ij} are the real and imaginary parts of R_{ij}. Steady-state solutions can be obtained by considering $R_{11} = 1 - R_{22} - R_{33}$, $R_{ij} = R_{ji}^*$, $W_{31} = 1$, and $\Delta_1 = 0$, in the form of $M\Psi = -I$, through the coefficient matrix method, where:

$$M = \begin{bmatrix} 0 & 0 & 0 & 0 & 0 & -2g_2 & -W_{21} & W_{32} \\ 0 & 0 & 0 & 2g_1 & 0 & 2g_2 & 0 & -(W_{32}+1) \\ -\Delta_2 & \gamma_{12} & -g_2 & 0 & g_1 & 0 & 0 & 0 \\ \gamma_{12} & \Delta_2 & 0 & g_2 & 0 & g_1 & 0 & 0 \\ 0 & g_2 & \gamma_{13} & 0 & 0 & 0 & 0 & 0 \\ -g_2 & 0 & 0 & \gamma_{13} & 0 & 0 & g_1 & 2g_1 \\ 0 & g_1 & 0 & 0 & -\gamma_{23} & \Delta_2 & 0 & 0 \\ g_1 & 0 & 0 & 0 & -\Delta_2 & -\gamma_{23} & g_2 & -g_2 \end{bmatrix} \tag{11}$$

and

$$I = \begin{pmatrix} 0 & 0 & 0 & 0 & 0 & g_1 & 0 & 0 \end{pmatrix}^T, \tag{12}$$

where the dispersion (α_{ij}) and absorption (β_{ij}) coefficients are given in the Appendix. Note that all the parameters in our calculations have been normalized to γ.

2.2 Main Model

The schematic of the micro-ring resonator, in which media that includes quantum interference effects is confined, is displayed in Fig. (1.b). The resonator has two inputs: one at the top from a straight waveguide and the other at the bottom of the ring. The quantum interference effects we consider involve a three-level atomic medium whose levels are coupled by two laser beams under the Λ-type coupling pattern, as illustrated schematically in Fig. (1.a) with decay mechanisms. States $|1\rangle$ and $|2\rangle$ are the ground and metastable states, respectively, while state $|3\rangle$ is an excited state. The transitions $|1\rangle \rightarrow |3\rangle$ and $|2\rangle \rightarrow |3\rangle$ have opposite parity, while $|1\rangle \rightarrow |2\rangle$ has the same parity.

The maser field E circulates within the ring resonator, externally pumped by a continuous wave (CW) source proportional to P, and couples the metastable state $|2\rangle$ and the excited state $|3\rangle$. The pump field is coupled to the resonator from the top of the ring in Fig. (1.b), and after light-matter interaction, it propagates as field E. The micro-ring resonator, schematically shown in Fig. (1.b), is designed to keep the field E inside the resonator, repeating the light-matter interaction after each round trip of a photon along the ring. Meanwhile, the field E_1, after coupling the ground and excited states under a technique, is directed out of the resonator and does not circulate along the ring. This technique is effective when the field E_1 is prepared with polarization opposite to that of field E.

Identifying the field that should circulate within the ring and the field that must exit without circulating relies on the beam splitter embedded within the micro-ring resonator, indicated by the black lines at the ring's bottom in Fig. (1.b). Due to the significant frequency difference between E and E_1 [refer to Fig. (1.a)], they do not significantly influence each other, allowing any minor effects to be disregarded.

In the case where the response of the atomic medium is faster than the micro-resonator lifetime (fast-response condition) and in the anomalous dispersion regime, the dynamics of the beam propagating in such a resonator are described in the mean-field limit with the Lugiato-Lefever equation (LLE) [31]:

$$\partial_t E = P - (1 + i\theta)E + (2C)iR_{23} + i\nabla^2 E, \tag{13}$$

where ∂_t represents the slow time over multiple round trips within the resonator. P denotes the amplitude of the input pump and is a fraction of field E, and θ indicates the detuning between the cavity resonant frequency and input frequency, which we use as the control parameter in our simulations. The transverse diffraction of the master field in two dimensions is described using the Laplacian. Finally, $2C$ describes the cooperativity parameter of the light-matter interaction, given by

$$2C = \frac{N\mu^2 kL}{2\hbar\gamma\varepsilon_0 T}, \tag{14}$$

where μ represents the transition dipole moment, k denotes the field wave number, L is the resonator length, γ describes the atomic linewidth, ε_0 indicates the permittivity of free space, and T is the resonator transmissivity. Every physical parameter in Eq. (13) has been scaled through appropriate normalizations, per standard methods for operating the mean-field or LLE model [31].

Details of the spatio-temporal dynamics of such a model are provided in Refs. [23, 25]. In this work, we ignore any spatial dependence of the field within the resonator; in fact, we consider the classical field circulating inside the ring resonator to be homogeneous and ignore the transverse diffraction of the field, setting the diffraction operator in Eq. (13) to $\nabla^2 = 0$. This reduction simplifies the system's dynamics from spatio-temporal to temporal, allowing us to investigate the evolution of temporal oscillations and optical instabilities as the detuning θ is varied as a control parameter.

We focus on the evolution of the driving field coupling states $|3\rangle \rightarrow |2\rangle$ [see Fig. (1.a)]. We also consider a fast medium where the atomic variables (level populations and coherences) quickly relax to their stationary values. This allows light propagating through the medium to experience absorption (gain) and refraction characterized by the density matrix element R_{23}. We utilize the expression for R_{23} (see Appendix) for the nonlinear response in the ring resonator, where the dynamics of the field E are described by the mean-field equation.

As mentioned above, our goal is to study optical instabilities in an all-optical bistable system. To do this, we first need to find homogeneous stationary solutions (HSS) derived from Eq. (13) by setting $\partial_t = 0$ and $\nabla^2 = 0$:

$$|P|^2 = \left[(1 + 2C\mathrm{Im}(\chi))^2 + (\theta - 2C\mathrm{Re}(\chi))^2\right]|E_s|^2, \tag{15}$$

where $\mathrm{Re}(\chi)$ and $\mathrm{Im}(\chi)$ are the real and imaginary parts of the electric susceptibility in R_{12} (see Appendix). We also set $2C = 30$ and use the resonator detuning θ as the control parameter of the atom-field-resonator system, as is commonly done in experiments. The values of Δ_2, W_{32}, W_{21}, P, and E_1 will be chosen based on the regime of interest later.

In our simulations, we employed the second order Runge Kutta algorithm to integrate Eq. (13) self consistently without the diffraction operator. We must highlight that we incorporated the coherence term (off-diagonal density matrix element) into the mean field using steady-state solutions (see Appendix).

3 Results and Discussion

As shown schematically in Fig. (1.a), we are interested in the evolution of the driving field coupling states $|2\rangle \rightarrow |3\rangle$ (denoted as E) with the Rabi frequency g_2. One of the fascinating predictions from [30] regarding Λ and Ξ atomic configurations is the amplification of a weak probe field across a broad frequency ranges of the absorption feature. In this study, the three-level atoms play the role of active medium. This occurs when the dressed atomic states are driven towards an inverted state, which necessitates fulfilling the condition [30].

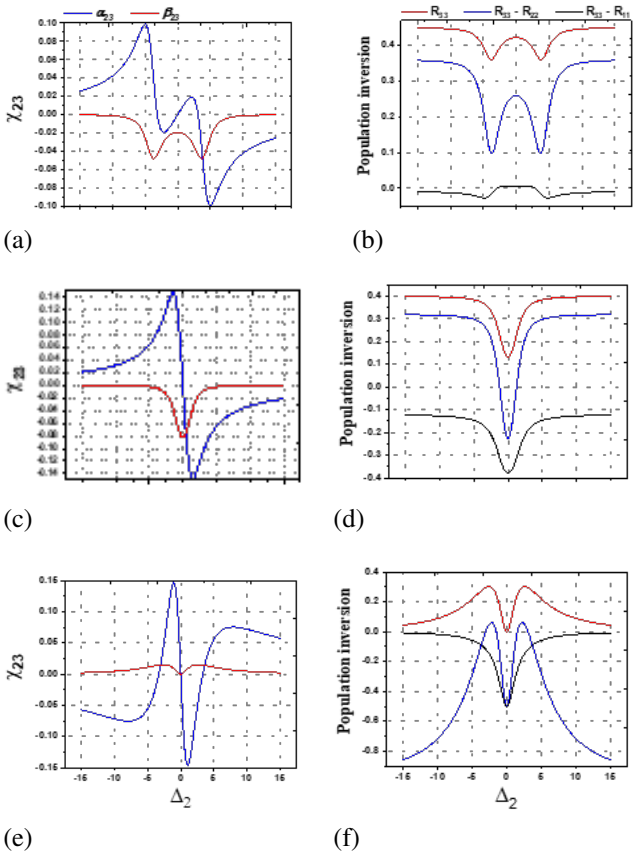

Figure 2: The electric susceptibility and Population inversion in the two allowed transitions and population of the exited state versus the material detuning. (a, b) gain in the presence of inversion $W_{21} = 0.5$, $W_{32} = 0.1$, $E_1 = 4$, $E = 1$, (c, d) gain in absence of inversion with $W_{21} = 0.5$, $W_{32} = 0.1$, $E_1 = E = 1$ and (e, f) inversion without gain $W_{21} = 0$, $W_{32} = 0.1$, $E_1 = E = 1$.

The findings from [30] regarding Λ and Ξ atomic configurations highlight the amplification of a weak probe field across a broad frequency range of the absorption feature. In this study, the three-level atoms function as the active medium. This amplification occurs when the dressed atomic states are driven towards an inverted state, which necessitates fulfilling the condition [30]:

$$\frac{W_{21} - W_{32}}{1 + W_{21}} > \left(\frac{E}{E_1}\right)^2, \tag{12}$$

This phenomenon significantly differs from what is typically observed in two-level systems. Firstly, two-level atoms generate gain rather than absorption in response to a probe, but only within specific frequency ranges. Secondly, it involves a parametric energy transfer from the pump to the probe, mediated by atomic susceptibility. On the other hand, for the three-level system, the gain arises from an inversion state between the levels of the excited atoms.

Based on condition (12), as shown in Fig. 2, we have identified and explored three regimes of operation depending on the population decay rate of level $|2\rangle$ to level $|1\rangle$ and the ratio of the driving field amplitudes:

i) Gain with population inversion in the $|2\rangle \rightarrow |3\rangle$ transition,
ii) Gain without population inversion (this is similar to lasing without inversion),
iii) Population inversion without gain.

Fig. 2 shows the steady-state solutions for absorption, dispersion profile, and population inversion along Δ_2. If we follow condition (12), then gain ($\beta_{23} < 0$) is achievable in the presence of population inversion ($R_{33} - R_{22} > 0$ & $R_{33} - R_{11} > 0$) [refer to Figs (2.a) and (2.b)]. However, if we relax the strict condition of Eq. (12) when choosing the strength of the driving fields, we arrive at a situation where population inversion ($R_{33} - R_{22} < 0$ & $R_{33} - R_{11} < 0$) is reversed around the resonance while gain ($\beta_{23} < 0$) is still established. In Figs (2.c) and (2.d), we have chosen equal values for the driving fields $E_2 = E_1 = 1$ while keeping the other parameters the same as in Figs (2.a) and (2.b). It is observed that around the resonance of the $|2\rangle \rightarrow |3\rangle$ transition, population inversion is absent but is obtained everywhere when Δ_2 moves far from resonance. The next regime, shown in Figs (2.e) and (2.f), is realized when no population decay is allowed from level $|2\rangle$ to level $|1\rangle$ (i.e., $W_{21} = 0$). In this case, gain is removed everywhere while population inversion can still be obtained far from the resonance of the $|3\rangle \rightarrow |2\rangle$ transition, a phenomenon that has been extensively studied. This also represents the "Raman transition," the result of which is coherent population trapping, and is realized when the population decay rate of level $|2\rangle$ to level $|1\rangle$ is considered zero ($W_{21} = 0$). In Fig. 3, the homogeneous stationary states (HSS) evolve with cavity detuning θ at the maximum gain, i.e., $\Delta_2 = 0.467$, according to Eq. (15), where a clear bistability is seen for negative cavity detuning values. In this study, our results are based on the values of

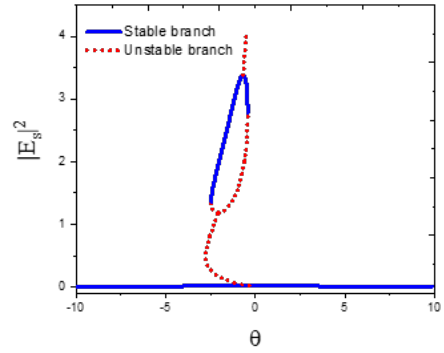

Figure 3: Bistability of the HSS in terms of cavity detuning. Parameter values are similar to Figs (2.c) and (2.d) with $\Delta_2 = 0.467$.

the parameters in the regime of gain without inversion, similar to lasing without inversion. As mentioned, we keep Δ_2 in the region where no inversion is expected while the gain is close to its maximum value. A wide bistability is obtained for the HSS solutions. The stable and unstable branches of The solutions are clearly defined. At $\theta = -2.462$, the system switches from the lower branch to the upper branch, and at $\theta = -0.425$ from the upper branch to the lower branch of the bistable diagram, or vice versa, so the bistable threshold is in the form of $-2.462 < \theta < -0.425$.

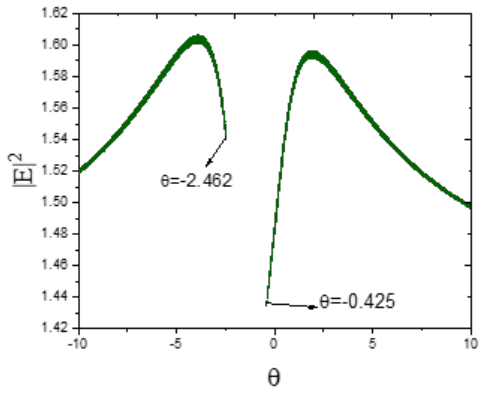

Figure 4: Field intensity, under the adiabatic scan of the resonator detuning. The parameter values in this figure are similar to those in Fig. 3.

In Fig. 4, we simulated the time-dependent field E based on Eq. (14) and kept the parameter values similar to Figs (3.c) and (3.d); we started the simulation from noise under the adiabatic scan $-10 < \theta < 10$. The simulation result and the homogeneous stationary solutions coincide and show a clear range for the bistable threshold and self-pulsing solutions. During the scan of the control parameter, only a period-one path for the field intensity appears, which is representative of the limit cycle. This oscillation disappears at the bistable threshold, which is due to the absence of Hopf instability in the upper branch of the HSS solutions.

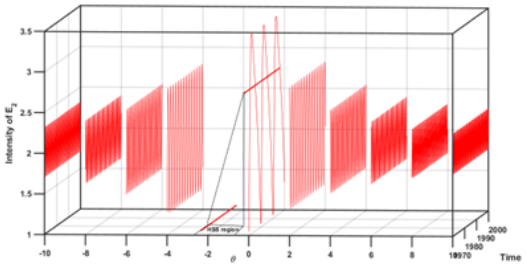

(a)

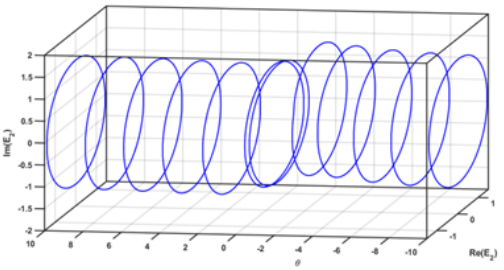

(b)

Figure 5: (a) Time trace, and (b) The limit cycle continuation from the Hopf (H) point at the very onset of instability on the lower branch of the OB curve shown in Fig. 3. Parameter values are similar to Fig. 3.

Figs (5.a) and (5.b) show the intensity-time and phase space of the field, respectively. From Fig. (5.a), it is concluded that from negative and positive values of θ, the oscillation frequency decreases and increases, respectively, at the bistable threshold due to moving away from the Hopf instability point in the lower branch. Fig. (5.b) shows the phase space of the complex field, which illustrates the limit cycles in the range of $-10 < \theta < 10$, where the radius of the cycles increases as the bistable threshold is approached, indicating an increase in the amplitude of oscillations in this range.

Bistability for input (P) and output (E_s) field intensities is shown in Fig. 6. Under a certain value of the input field, by increasing or decreasing θ as a control parameter, the output field increases and decreases respectively. The boundary of these changes is the bistable threshold of Fig. 3, which is the same interpretation for the other side. Thus, by reducing or increasing θ, the output intensity value can be controlled under the input intensity.

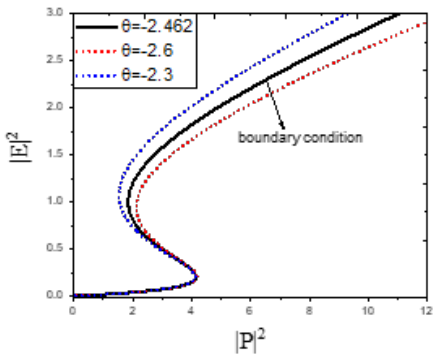

Figure 6: Bistability in the input and output intensities with $\theta = -2.462$ as a boundary condition. Other parameter values in this figure are similar to those in Fig. 3.

4 Conclusions

Our results indicate that the intensity of the output field from the micro-ring resonator, influenced by quantum interference effects, exhibits oscillations if the fields used to couple the atomic levels are considered continuous waves (CW). This behavior arises from the Hopf instability in the lower branch of the bistable dia-gram, attributed to the gain present in this regime. We identified a single type of periodic solution (one-periodic with a limit cycle) in the system dynamics, as we considered a fast medium where the atomic varia-bles (level populations and coherences) quickly relax to their stationary values, facilitating the propagation of light through the medium. Notably, we demonstrated a system with self-oscillating dynamics by exploring the gain regime without population inversion, which allows for utilization in all-optical communication and cir-cuits. Furthermore, we provide evidence that the output intensity of the resonator can be controlled by adjusting the resonator detuning.

Acknowledgements We gratefully acknowledge Dr. Mansour Eslami for his valuable guidance and insights.

Appendix

It should be mentioned that off-diagonal variables being complex are written in the following form:

$$R_{23} = \alpha_{23} + i\beta_{23}, \tag{A1}$$

$$R_{13} = \alpha_{13} + i\beta_{13}, \tag{A2}$$

$$R_{12} = \alpha_{12} + i\beta_{12}, \tag{A3}$$

which are proportional to the field amplitude E_1 and E via [29]:

$$R_{23} = \chi_{23}E, \tag{A4}$$

$$R_{12} = \chi_{13}E_1, \tag{A5}$$

In this section, we solve the coefficients matrix (Eq. (10)) using MATLAB software and obtain the absorption and dispersion coefficients for the transition between the levels, as well as the population equations for all three levels, and in a simplified form, we have:

$$\begin{aligned}
D = {} & 2g_2g_1^6\gamma_{13}(2W_{21}+W_{32}) + g_2(W_{21}\gamma_{13}^2 + 2g_2^2\gamma_{13} + W_{21}W_{32}\gamma_{13}^2 - 8W_{21}\Delta_2^2\gamma_{13} - 4W_{32}\Delta_2^2\gamma_{13})g_1^4 \\
& + g_2(-6W_{21}g_2^2\gamma_{13} + 4W_{21}g_2^2\gamma_{23} + 2W_{32}g_2^2\gamma_{13} + 2W_{32}g_2^2\gamma_{23} + 12g_2^2\gamma_{12}\gamma_{13})g_1^4 + g_2(8W_{21}\gamma_{12}\gamma_{13}\gamma_{23} + 4W_{32}\gamma_{12}\gamma_{13}\gamma_{23} \\
& + 2g_2^4\gamma_{13} + 2g_2^4\gamma_{23} - 2W_{21}\Delta_2^2\gamma_{13}^2)g_1^2 + g_2(-2\Delta_2^2g_2^2\gamma_{13} + 2g_2^2\gamma_{12}\gamma_{13}^2 + 4W_{21}\Delta_2^4\gamma_{13} + 2W_{32}\Delta_2^4\gamma_{13} \\
& + 2W_{21}g_2^4\gamma_{13})g_1^2 + g_2(-6W_{21}g_2^4\gamma_{23} + 2W_{32}g_2^4\gamma_{23} + 12g_2^4\gamma_{12}\gamma_{23} + 2W_{21}g_2^2\gamma_{13}\gamma_{23} + 2W_{21}\gamma_{12}\gamma_{13}^2\gamma_{23})g_1^2 \\
& + g_2(2g_2^2\gamma_{12}\gamma_{13}\gamma_{23} - 2W_{21}W_{32}\Delta_2^2\gamma_{13}^2 + 4W_{21}\Delta_2^2g_2^2\gamma_{12} + 6W_{21}\Delta_2^2g_2^2\gamma_{13} + 2W_{32}\Delta_2^2g_2^2\gamma_{12})g_1^2 \\
& + g_2(-2W_{32}\Delta_2^2g_2^2\gamma_{13} + 4W_{21}\Delta_2^2\gamma_{12}^2\gamma_{13} + 4W_{21}\Delta_2^2\gamma_{13}\gamma_{23}^2 + 2W_{32}\Delta_2^2\gamma_{12}^2\gamma_{13} + 2W_{32}\Delta_2^2\gamma_{13}\gamma_{23}^2)g_1^2 \\
& + g_2(2W_{21}g_2^2\gamma_{12}\gamma_{13}^2 + 4W_{21}g_2^2\gamma_{12}\gamma_{23}^2 + 2W_{32}g_2^2\gamma_{12}\gamma_{23}^2 + 4W_{21}\gamma_{12}^2\gamma_{13}\gamma_{23}^2 + 2W_{32}\gamma_{12}^2\gamma_{13}\gamma_{23}^2)g_1^2 \\
& + g_2(12\Delta_2^2g_2^2\gamma_{13}\gamma_{23} + 12g_2^2\gamma_{12}^2\gamma_{13}\gamma_{23} + 2W_{21}W_{32}g_2^2\gamma_{13}\gamma_{23} + 2W_{21}W_{32}\gamma_{12}\gamma_{13}^2\gamma_{23}^3 - 6W_{21}g_2^2\gamma_{12}\gamma_{13}\gamma_{23})g_1^2 \\
& + g_2(2W_{32}g_2^2\gamma_{12}\gamma_{13}\gamma_{23} + 2g_2^6\gamma_{23} + W_{21}\Delta_2^2g_2^4 + W_{21}\Delta_2^4\gamma_{13}^2 + W_{21}g_2^4\gamma_{23}^2) + g_2(2W_{21}g_2^6\gamma_{23} + W_{21}\Delta_2^2\gamma_{12}^2\gamma_{13}^2 \\
& + W_{21}\Delta_2^2\gamma_{13}^2\gamma_{23}^2 + W_{21}\gamma_{12}^2\gamma_{13}^2\gamma_{23}^2 + 2\Delta_2^2g_2^2\gamma_{13}^2\gamma_{23}) + g_2(2g_2^2\gamma_{12}^2\gamma_{13}\gamma_{23} + 4g_2^4\gamma_{12}\gamma_{13}\gamma_{23} + W_{21}W_{32}\Delta_2^2g_2^4 \\
& + W_{21}W_{32}\Delta_2^4\gamma_{13}^2 + W_{21}W_{32}g_2^4\gamma_{23}^2) + g_2(2W_{21}\Delta_2^2g_2^2\gamma_{12}\gamma_{13} + 2W_{21}g_2^2\gamma_{12}\gamma_{13}\gamma_{23}^2 + W_{21}W_{32}\Delta_2^2\gamma_{12}^2\gamma_{13}^2 + W_{21}W_{32}\Delta_2^2\gamma_{13}^2\gamma_{23}^2 \\
& + W_{21}W_{32}\gamma_{12}^2\gamma_{13}^2\gamma_{23}^2) + g_2(2W_{21}\Delta_2^2g_2^2\gamma_{13}^2\gamma_{23} + 2W_{21}\gamma_{12}^2\gamma_{13}^2\gamma_{23} + 4W_{21}g_2^4\gamma_{12}\gamma_{13}\gamma_{23}) + 2W_{21}W_{32}\Delta_2^2g_2^2\gamma_{12}\gamma_{13} \\
& + 2W_{21}W_{32}g_2^2\gamma_{12}\gamma_{13}\gamma_{23}^2
\end{aligned} \tag{A6}$$

$$\begin{aligned}\tilde{\alpha}_{23} = \Delta_2 g_2 \{ & g_1^4 \gamma_{13}(W_{21} - W_{32}) + 2(W_{32} - W_{21}) \\ & \times \left(g_2^2 \gamma_{12} + \Delta_2^2 \gamma_{13}\right) + 2(W_{32} - W_{21}) \gamma_{12}^2 \times \gamma_{13} \\ & - g_2 \left[(1 + W_{21}) \times \gamma_{13} - (W_{32} + 1) \times W_{21}\right] \\ & - W_{21} \times \gamma_{12}(\gamma_{13} + \gamma_{23}) \\ & - W_{21} W_{32} \times \gamma_{13}(\gamma_{12} + \gamma_{23}) g_1^2 \}\end{aligned} \tag{A7}$$

$$\begin{aligned}\tilde{\beta}_{23} = & g_1^4 g_2 \gamma_{13} \left[2\gamma_{12}(W_{32} - W_{21}) - W_{21}(W_{32} + 1)\right] \\ & + \left[g_2 W_{21}(\Delta_2^2 \gamma_{13} - g_2^2 \gamma_{23})(W_{32} + 1)\right. \\ & + 2 g_2 \gamma_{23}(W_{32} - W_{21})(g_2^2 \gamma_{12} + \Delta_2^2 \gamma_{13} + \gamma_{12}^2 \gamma_{13}) \\ & \left. - (W_{32} + W_{21}) g_2 \gamma_{12} \gamma_{13} \gamma_{23}\right] g_1^2,\end{aligned} \tag{A8}$$

$$\begin{aligned}\tilde{\alpha}_{13} = & g_1^3 g_2^2 \left[2W_{32}\Delta_2(\gamma_{12} + \gamma_{23}) - W_{21}\Delta_2 \times \right. \\ & \left. (W_{32} + 2\gamma_{12} + 2\gamma_{23} + 1)\right] + g_1 g_2^2 \Delta_2 \times \\ & \left[W_{21}\left(\Delta_2^2(1 + W_{32}) + \gamma_{23}^2(1 + W_{32})\right)\right. \\ & \left. + 2 g_2^2 \gamma_{23}(1 + W_{21})\right],\end{aligned} \tag{A9}$$

$$\begin{aligned}\tilde{\beta}_{13} = & g_1^5 (W_{21}\gamma_{13})(1 + W_{32}) + g_1^3 \left[W_{21}(1 + W_{32})\right. \\ & \times \left(g_2 \gamma_{23} + 2\gamma_{13}(\gamma_{12}\gamma_{23} - \Delta_2^2)\right) \\ & \left. + 2 g_2^2 \gamma_{12} \gamma_{13}(1 + W_{21})\right] \\ & + g_1 \left[(1 + W_{21})\left(2 g_2^4 \gamma_{12}\gamma_{23} + 4 g_2^2 \gamma_{13}\gamma_{23}\right)\right. \\ & \times \left(\Delta_2^2 + \gamma_{12}^2\right) \\ & + W_{21}\gamma_{13}(1 + W_{32})\left(\Delta_2^4 + (\gamma_{12}\gamma_{23})^2\right) \\ & \left. + g_2^2 W_{21}\gamma_{12}(\Delta_2^2 + \gamma_{23}^2)\right] \\ & + W_{21}\Delta_2^2 \gamma_{13}(\gamma_{12}^2 + \gamma_{23}^2),\end{aligned} \tag{A10}$$

$$\begin{aligned}\tilde{\alpha}_{12} = g_1 g_2 \{ & (W_{21} - W_{32}) \times (2\gamma_{13} g_1^4 + 2 g_1^2 g_2^2 \gamma_{23}) \\ & + \gamma_{13} g_1^2 \times (2\gamma_{12}\gamma_{23} - 2\Delta_2^2) \\ & - (W_{21} + 1) \times (2 g_1^2 g_2^2 \gamma_{13} + 2 g_2^4 \gamma_{23}) \\ & + g_2^2 \times (\gamma_{12}\gamma_{13}\gamma_{23}) - (1 + W_{32}) \\ & \times (\gamma_{13} g_1^2 W_{21}\gamma_{23} - g_2^2 W_{21}\Delta_2^2) \\ & - W_{21}\gamma_{12}\gamma_{13} \times (\gamma_{23}^2 + \Delta_2^2)\} + W_{21} + \gamma_{23}^2,\end{aligned} \tag{A11}$$

$$\begin{aligned}\tilde{\beta}_{12} = & g_1^3 g_2 \Delta_2 \gamma_{13} \left[W_{21} \times (1 + W_{32} + 2(\gamma_{12} + \gamma_{23}))\right. \\ & \left. - 2W_{32} \times (\gamma_{12} + \gamma_{23})\right] \\ & - g_1 g_2 \times (1 + W_{32}) W_{21}\Delta_2\gamma_{13} \times (\Delta_2 + \gamma_{23}^2) \\ & + 2 g_1 g_2 \times (1 + W_{21})(\Delta_2 \gamma_{13}\gamma_{23}),\end{aligned} \tag{A12}$$

$$\begin{aligned}\tilde{R}_{22} = & 2 g_1^6 W_{32}\gamma_{13} + g_2 g_1^4 \left(2 g_2^2 \gamma_{13} \times (1 + 2\gamma_{12})\right. \\ & + 2W_{32} \times \left(g_2^2 \gamma_{23} + 2\gamma_{12}\gamma_{13}\gamma_{23} - 2\Delta_2^2 \gamma_{13})\right) \\ & + g_2 g_1^2 \left[2W_{32} \times \left(\gamma_{13}\Delta_2^2(\Delta_2^2 + \gamma_{23}^2)\right)\right. \\ & + g_2^2 \gamma_{12}(\Delta_2^2 + \gamma_{23}^2) + \gamma_{13}\gamma_{12}^2(\Delta_2^2 + \gamma_{23}^2)\left.\right] \\ & + 4\gamma_{13}\Delta_2^2 g_2^2 \gamma_{23} + (1 + 2\gamma_{12}) \times 2 g_2^4 \gamma_{23} \\ & \left. + 2 g_2^2 \gamma_{13} \times \left(\gamma_{12}\gamma_{23} + 2\gamma_{12}^2 \gamma_{23} - \Delta_2^2\right)\right],\end{aligned} \tag{A13}$$

$$\begin{aligned}\tilde{R}_{33} = & 2W_{21} g_1^6 g_2 \gamma_{13} + g_1^4 g_2 \left(2W_{21} g_2^2 (\gamma_{23} - \gamma_{13})\right. \\ & + 4\gamma_{13} \times (W_{21}(\gamma_{12}\gamma_{23} - \Delta_2^2) + g_2^2 \gamma_{12})\left.\right) \\ & + g_2 \left[2W_{21} \times \left(\gamma_{13}\Delta_2^4 + \Delta_2^2 g_2^2 \gamma_{12} + g_2^2 \gamma_{12}\gamma_{23}^2\right.\right. \\ & + \gamma_{13}\gamma_{12}^2 \gamma_{23^2} + \gamma_{13}\Delta_2^2 \gamma_{23}^2 - \gamma_{13} g_2^2 \gamma_{12}\gamma_{23}\left.\right) \\ & \left. + \gamma_{13}\Delta_2^2(g_2^2 + \gamma_{12}^2)\right] + 4 g_2^2 \gamma_{13}\gamma_{23} \\ & \times (\Delta_2^2 + \gamma_{12}^2) + 2 g_2^4 \gamma_{23} \times (2\gamma_{12} - W_{21})\left.\right] g_1^2.\end{aligned} \tag{A14}$$

$$R_{ii} = \frac{\tilde{R}_{ii}}{D}, \tag{A15}$$

$$\alpha_{ij} = \frac{\tilde{\alpha}_{ij}}{D}, \tag{A16}$$

$$\beta_{ij} = \frac{\tilde{\beta}_{ij}}{D}, \tag{A17}$$

References

1. F. T. Arecchi and R. G. Harrison, *Instabilities and Chaos in Quantum Optics*, Springer Science, 2012.
2. H. Haken, Zeitschrift für Physik, **190**, 3, (1966)
3. A. Joshi and M. Xiao, J. Modern Opt. **57**, 14, (2010)
4. G. Khitrova, J. Valley, and H. Gibbs, Phys. Rev. Lett. **60**, 12 (1988)
5. L. A. Lugiato et al., Opt. Commun. **43**, 4, (1982)
6. G. H. Van Tartwijk and G. P. Agrawal, Prog. in Quant. Elec. **22**, 2 (1998)
7. K. Osman and Joshi, Phys. Lett. A, **376**, 37 (2012)
8. L. Orozco et al., Phys. Rev. A, **39**, 3 (1989)
9. C. Savage, H. Carmichael, and D. Walls, Opt. Comm., **42**, 3 (1982)
10. P. Grangier, J. Roch, J. Roger, L. Lugiato, E.M. Pessina, G. Scandroglio, and P. Galatola, Phys. Rev. A, **46**, (1992)
11. W. Yang, Joshi, and M. Xiao, Phys. Rev. Lett., **95**, 9 (2005)
12. H. M. Gibbs et al., Phys. Rev. Lett., **46**, 7 (1981)

13. M. Fleischhauer, Imamoglu, and J. P. Marangos, Rev. Mod. Phys., **77**, 2 (2005)
14. K. J. Boller, Imamoğlu, and S.E. Harris, Phys. Rev. Lett., **66**, 20 (1991)
15. S. E. Harris, Phys. Today, **50**, 7 (1997)
16. Kasapi et al., Phys. Rev. Lett., **74**, 13 (1995)
17. Rosenberger, L. Orozco, and H. Kimble, Phys. Rev. A, **28**, 4 (1983)
18. N. V. Vitanov et al., Rev. Mod. Phys., **89**, 1 (2017)
19. M. O. Scully, Phys. Rev. Lett., **67**, 14 (1991)
20. J. Mompart, C. Peters, and R. Corbalán, Phys. Rev. A, **57**, 3 (1998)
21. Vladimirov et al., Phys. Rev. E, **57**, 2 (1998)
22. M. Eslami et al., Phys. Rev. A, **108**, 5 (2023)
23. M. Eslami et al., Phys. Rev. A, **90**, 2 (2014)
24. M. Eslami, R. Kheradmand, and G. Oppo, J. Phys. B: At. Mol. Opt. Phys., **53**, 7 (2020)
25. G. L. Oppo, J. Mod. Opt., **57**, 14-15 (2010)
26. G. L. Oppo, D. Grant, and M. Eslami, Phys. Rev. A, **105**, 1 (2022)
27. H. Babu and H. Wanare, Phys. Rev. A, **88**, 2 (2013)
28. H. Babu and H. Wanare, Phys. Rev. A, **83**, 3 (2011)
29. M. O. Scully and M. S. Zubairy, *Quantum optics* (Cambridge University Press, 1997).
30. Manka et al., Phys. Rev. A, **43**, 7 (1991)
31. M. Haelterman, S. Trillo, and S. Wabnitz, Opt. Comm., **91**, 5-6 (1992)